UNIVERSITY OF TARTU
Faculty of Science and Technology
Institute of Physics

Kristina Raudonen

SYNTHESIS, ANALYSIS, AND APPLICATION OF GRAPHENE LAYERS FOR FUNCTIONAL DEVICES

Bachelor's Thesis (12 ECTS)

Curriculum Science and Technology

Supervisors:
Professor, PhD. Kaupo Kukli
Engineer, MSc. Tauno Kahro

Tartu 2022

SYNTHESIS, ANALYSIS, AND APPLICATION OF GRAPHENE LAYERS FOR FUNCTIONAL DEVICES

Abstract:

The study is devoted to qualitative analysis of monolayer graphene deposited onto a metal catalyst and transferred onto substrates with different adhesive properties. In addition, qualitative analysis of graphene formed by annealing amorphous carbon with a nickel carbon diffusion layer was conducted. Some applications together with analysis of transferred graphene in dielectric stacks in functional resistive switching devices were considered and investigated.

Keywords:

graphene, chemical vapor deposition, Raman spectroscopy, resistive switching

CERCS: P250, P260

GRAFEENIKIHTIDE SÜNTEES JA ANALÜÜS FUNKTSIONAALSETES SEADMETES KASUTAMISE EESMÄRGIL

Lühikokkuvõte:

Uurimistöö on suunatud metallkatalüüdi pinnale sadestatud ja seejärel erinevate adhesiooniomadustega substraatidele üle kantud monokihilise grafeeni kvalitatiivsele analüüsile. Lisaks sellele analüüsiti kvalitatiivselt grafeeni, mis formeeriti lõõmutades süsiniku difusiooni võimaldava nikli ja sellega kontakteeritud amorfse süsiniku kihte. Arvestati võimalustega kasutada ja katsetada grafeeni isoleerivate dielektrikkihtide vahel funktsionaalsetes takistuslülituslikes mäluseadmetes.

Võtmesõnad:

grafeen, keemiline aurufaassadestamine, Raman spektroskoopia, takistuslülitus

CERCS: P250, P260

TABLE OF CONTENTS

TERMS, ABBREVIATIONS AND NOTATIONS

CVD – Chemical Vapor Deposition.

sccm – Standard Cubic Centimetres per Minute. A unit for measurement of flow in standard conditions.

IPA – isopropyl alcohol, isopropanol, $(CH_3)_2CHOH$. Its IUPAC name is propan-2-ol.

PMMA – poly(methyl methacrylate), $(C_5O_2H_8)_n$. Its IUPAC name is poly(methyl 2-methylpropenoate). PMMA is a transparent thermoplastic, also known as acrylic glass, and dissolves well in organic solvents such as acetone or toluene.

SEM – Scanning Electron Microscope, used to view surfaces of samples, or in the present case, thin film surfaces.

XRR – X-Ray Reflectometry, used for evaluation of roughness, thickness, and density of different layers in a sample.

TEMAH - hafnium tetrakis(ethylmethylamide), $Hf[N(CH_3)(C_2H_5)]_4$, used to deposit HfO_2 oxide film in this work.

INTRODUCTION

A two-dimensional honeycomb lattice of carbon atoms forming a tightly packed flat monolayer, known as graphene, is a building block of graphitic materials such as one-dimensional carbon nanotubes and three-dimensional graphite. Prior to 2004, graphene was believed to be unstable and unable to exist as a free-standing material outside of a laboratory or 'academical' conditions (Geim and Novoselov, 2007). The use of silicon in the semiconductor industry was reaching its performance limits and so, when in 2004 Geim and Novoselov published an article where they had discovered a means to mechanically peel highly oriented pyrolytic graphite to obtain few-layer graphene, the focus could finally start shifting from silicon to graphene (Novoselov *et al.*, 2004). Researchers are still fine-tuning the properties of graphene, increasing the scale of its production techniques, as well as honing its potential applications (Al Faruque *et al.*, 2021).

In addition to the electronics industry, fields in which graphene is utilized include agriculture and wastewater management, the biomedical industry. In the electronics industry, graphene may be used, for example, in solar energy, wearable technology, and automobile, aerospace, and marine industry. Currently the most astonishing applications of graphene-based materials are supercapacitors, nanomembranes for wastewater treatment, Li-ion batteries, microbial fuel cells, sensors, and solar cells (Al Faruque *et al.*, 2021).

Although there are many popular graphene manufacturing methods, such as chemical vapor deposition (Song *et al.*, 2021), liquid phase exfoliation of graphite into graphene (Tung *et al.*, 2016), reduction of graphene oxide (Pei and Cheng, 2012; Alazmi *et al.*, 2016) and mechanical exfoliation (Yi and Shen, 2015), the cost of large-scale high purity monolayer graphene production is a major constraint (Al Faruque *et al.*, 2021).

In this bachelor's thesis, the graphene was synthesized in two ways:

1. By chemical vapor deposition of carbon, degraded from methane at 1000 °C, onto a copper metal catalyst.
2. By annealing amorphous carbon at 1000 °C, causing it to dissolve into a carbon diffusion layer made of nickel and crystallize into graphene outside of the nickel upon cooling.

Graphene synthesized by the first method was transferred onto substrates with different wettability to analyse their effects on the graphene quality, as well as transferred into dielectric

stacks to analyse the effect of graphene on the electrical performance, more specifically the resistive switching capability, of such devices.

The latter synthesis method was done to form graphene directly onto the desired substrate to exclude the need to transfer graphene from the metal catalyst to the substrate, as in the first synthesis method, and eliminate the possible introduction of defects from handling graphene during the transfer process.

1 LITERATURE REVIEW

1.1 Properties and some applications of graphene

Graphene consists of a single atomic layer of carbon particles forming a two-dimensional hexagonal lattice structure. Monolayer graphene is the thinnest material in the world, with a thickness of only 0.334 nm. Due to its crystal structure, graphene has remarkable thermal and electrical conductivity as well as a sizeable specific surface area (Ren *et al.*, 2018). Despite being the thinnest, it is mechanically very strong and flexible, as well as transparent (Kim *et al.*, 2009).

Because of its unique properties, graphene has potential applications in a variety of areas such as flexible energy storage devices, semiconductor materials, drug carriers, photoelectric devices, wearable technologies and many more (Ren *et al.*, 2018). Due to its transparency, graphene can be used as an electrode in liquid crystal displays (LCD) and organic light-emitting displays (OLED). On the other hand, large specific surface area of graphene allows it to be used in sensors such as gas detectors (Nguyen *et al.*, 2013). Graphene has also been studied as a potential superconductor, with the aim to increase the temperature required to achieve the superconducting state (Di Bernardo *et al.*, 2017; Liu *et al.*, 2017).

Despite the wide variety of graphene applications, this work contains mainly applications of graphene in resistive switching devices.

Resistive random-access memory, also known as ReRAM or memristor, operates on the principle of resistive switching between two bi-stable resistance states: a high resistance state (HRS) and a low resistance state (LRS). The HRS state is also known as the ‘OFF’ state, while the LRS is known as the ‘ON’ state. In ReRAM devices, the OFF-to-ON transition is triggered by voltage-biasing and is designated as a ‘SET’ event. The opposite ON-to-OFF transition, known as a ‘RESET’ event, is triggered by applying voltage of the same or opposite polarity to the SET event, where the former occurs in unipolar devices, and the latter in bipolar devices (Mannequin *et al.*, 2016).

In a device where resistive switching occurs, the desired hysteresis effect is achieved by the redistribution of ions. In oxide-based memristors this effect is theorised to occur due to migration of oxygen ions or oxygen vacancies. Typically, the migration is difficult to control as the ions can migrate across the area of the whole device, causing undesirable effects such as high leakage and operating currents, and instabilities in resistive switching performance. But,

by inserting a graphene layer within the device it can act as an ion-blocking barrier and thus, with the addition of intentional nanoscale defects in the graphene layer, the ion migration, which directs the resistive switching mechanism, can be tuned. In particular, by directing the ion migration to such graphene nanopores, the current needed for operation as well as RESET events is reduced (Lee *et al.*, 2016). Moreover, memristor devices containing graphene have been studied for multistate resistive switching, where the device has multiple stable resistance states and parallel operation processes can occur, meaning such a device could potentially store double the amount of data (Sun *et al.*, 2021).

In addition to investigating the effect of using graphene in resistive switching devices, the influence of annealing on the electrical properties of such graphene-containing devices will be analysed.

1.2 Graphene synthesis and transfer methods

The main method for synthesis of graphene which is used in this work is chemical vapor deposition, CVD. In this technique, through chemical reactions a solid thin film is deposited from a vapor species onto a substrate (Saeed *et al.*, 2020). In case of graphene deposition, the substrate is replaced with a metal catalyst, such as copper or nickel, which lowers the energy barrier of the reaction and consequently lowers the necessary reaction temperature. The presence of a metal catalyst not only lowers the energy needed for pyrolysis of the precursors, but also for the formation of the ordered hexagonal graphene structure. Without a metal catalyst, the formation of graphene on a substrate could need temperatures starting from 2500 °C, while with the use of a nickel or copper catalyst and, for example, a methane precursor, the temperature would range between 800 to 1000 °C (Miao *et al.*, 2011).

Typically, rather than using nickel, a copper catalyst is used when growing graphene with CVD. Because carbon solubility in nickel is non-negligible (Natesan and Kassner, 1973) it can cause carbon to dissolve into the nickel during deposition at high temperatures and later, during cooling, the dissolved carbon can resurface and cause unwanted deposition of carbon below the deposited graphene (Miao *et al.*, 2011). In copper such unwanted carbon deposition from the bottom of the graphene would not occur, as its carbon solubility is near-zero (López and Mittemeijer, 2004) even at 1000 °C. Before the deposition process is started, the copper must be annealed to increase the size of the grains and reduce the overall length of grain boundaries. Without prior annealing, the long grain boundaries would act as areas of high surface energy and cause more graphene growth along these grain boundaries. Thus, to achieve graphene of as uniform thickness as possible, it is important to minimize the grain boundaries as well as any

defects. Due to the polycrystalline nature of copper, the graphene also grows in a polycrystalline nature (Miao *et al.*, 2011).

During annealing and deposition steps, the use of hydrogen gas reduces the oxide layer on the metal catalyst and helps the growth of graphene by dehydrogenation of precursor gas and carbon radicals on the substrate surface (Saeed *et al.*, 2020).

Since the graphene in the CVD method is grown on a metal catalyst instead of a substrate with desired properties, the graphene must be transferred to a suitable substrate without introducing defects, such as wrinkles, nor breaking its structural integrity during the transfer process. This is a difficult task since the two-dimensional nature of graphene leads to strong surface interactions which affects its ability to adhere to a substrate. To improve the adhesion properties of graphene, wettability properties of the target substrate can be altered by plasma treating the substrate. Plasma treating should lead to surface activation of the substrate, resulting in increased surface activity and graphene transfer with less defects (Lukose *et al.*, 2021). For this reason, the effect of plasma-treated substrate on the quality of transferred graphene is analysed in this work.

Although depositing graphene onto a metal catalyst via CVD is a perfectly viable method to produce large-scale high-quality graphene, it is more desirable to eliminate the graphene transfer step and develop a method of direct formation of graphene onto the substrate. Such direct deposition can be attempted by manipulating a solid carbon source between nickel and substrate layers (Peng *et al.*, 2011). As mentioned before, nickel has non-negligible temperature-dependent carbon solubility, thus, when such a structure is heated at 1000 °C, the carbon atoms from the solid carbon source dissolve into the nickel. Upon cooling, the solubility of carbon in nickel decreases, hence the carbon atoms precipitate out of nickel and form a graphene sheet (Miao *et al.*, 2011). Since graphene sheets can form both above and below the nickel, as long as the nickel is dissolved alongside the overlying graphene, this method could be used to directly form transfer-free graphene onto the substrate (Peng *et al.*, 2011). Additionally, the location where the graphene sheet will form can be controlled by applying a carbon diffusion barrier. By depositing such a barrier layer onto the nickel, graphene formation at the substrate-nickel interface can be enhanced and the formation of graphene at the nickel and carbon diffusion barrier interface can be hindered (Kim *et al.*, 2018).

In the experimental part of this work, direct formation of graphene on suitable substrates is investigated alongside CVD-deposited graphene transferred onto fitting substrates.

1.3 Qualitative analysis of graphene

Since Raman spectroscopy is the main method for qualitative analysis of graphene in this thesis, a thorough explanation on its working principle and the information that can be gathered from a Raman spectrum is essential.

As a non-invasive and non-destructive technique, Raman spectroscopy is one of the most reliable qualitative analysis techniques available for structural characterization of graphitic materials, such as graphene. It works on the principle of inelastic scattering of monochromatic light caused by a laser source interacting with a sample. In Raman spectroscopy, the Raman scattered light can be analysed and information about the chemistry and structure of the material can be deduced. The most distinct features present in Raman spectra of almost all sp^2 materials are the G, 2D and D peaks (Saeed *et al.*, 2020). Their position, shape and intensity allow to distinguish different graphitic materials (Ferrari, 2007).

In Raman spectra, the G-band is positioned around 1580 cm^{-1} and shows the first order scattering that occurs in all pairs of sp^2 atoms due to bond stretching, while 2D and D bands show second order scattering. The 2D-band is positioned at around 2700 cm^{-1} and the D-band is characteristically present at ca. 1350 cm^{-1}. The appearance of a D-band implies the presence of disorder, such as defects in the lattice and broken symmetry (Ferrari, 2007; Warner *et al.*, 2013).

Raman spectroscopy is crucial for analysis of graphene as it can be used to determine its thickness. In a Raman spectrum of graphene with Bernal stacking, the 2D peak decreases in intensity, widens and is shifted to higher Raman shift values with increasing graphene thickness. While monolayer graphene has a single, sharp 2D peak, the thicker the graphene layers become, the more its 2D peak splits, starting to resemble a graphite spectrum (Saeed *et al.*, 2020). This phenomenon is visualized by Ferrari *et al* in Figure 1.

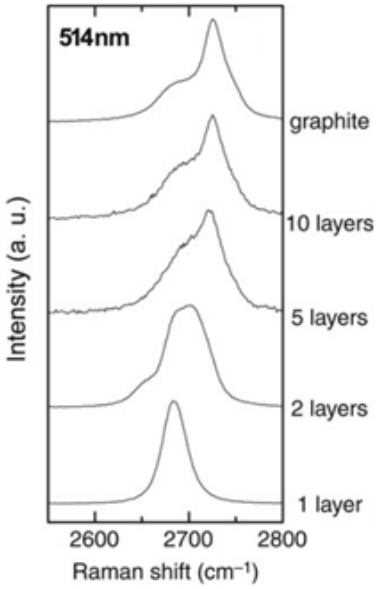

Figure 1. Raman spectra of graphite and graphene with different thickness, showing the 2D bands (Ferrari, 2007).

Raman spectroscopy can be used to analyse the quality of synthesized graphene and find the most optimal parameters for the deposition of monolayer graphene. The ratio of intensity of 2D to G peaks (I_{2D}:I_G), and full width at half maximum (FWHM) values can be used to assess the width and height of the peaks and in turn determine the graphene thickness (Kumar *et al.*, 2014). Typically, ratio of I_{2D}:$I_G \geq 2$ shows monolayer graphene, I_{2D}:$I_G < 1$ shows multilayer graphene, and I_{2D}:I_G values between these two show bilayer graphene (Nguyen *et al.*, 2013).

Figure 2 shows the results of an experiment by Kumar *et al.* on how fine-tuning the deposition temperature and gas flow rates can lead to higher quality monolayer graphene. According to the Raman spectra in this figure, the highest quality monolayer graphene was deposited at 1030 °C and at 3:30 gas flow ratio of CH_4 to H_2, which is confirmed by the corresponding highest I_{2D}:I_G ratios and lowest FWHM values (Kumar *et al.*, 2014).

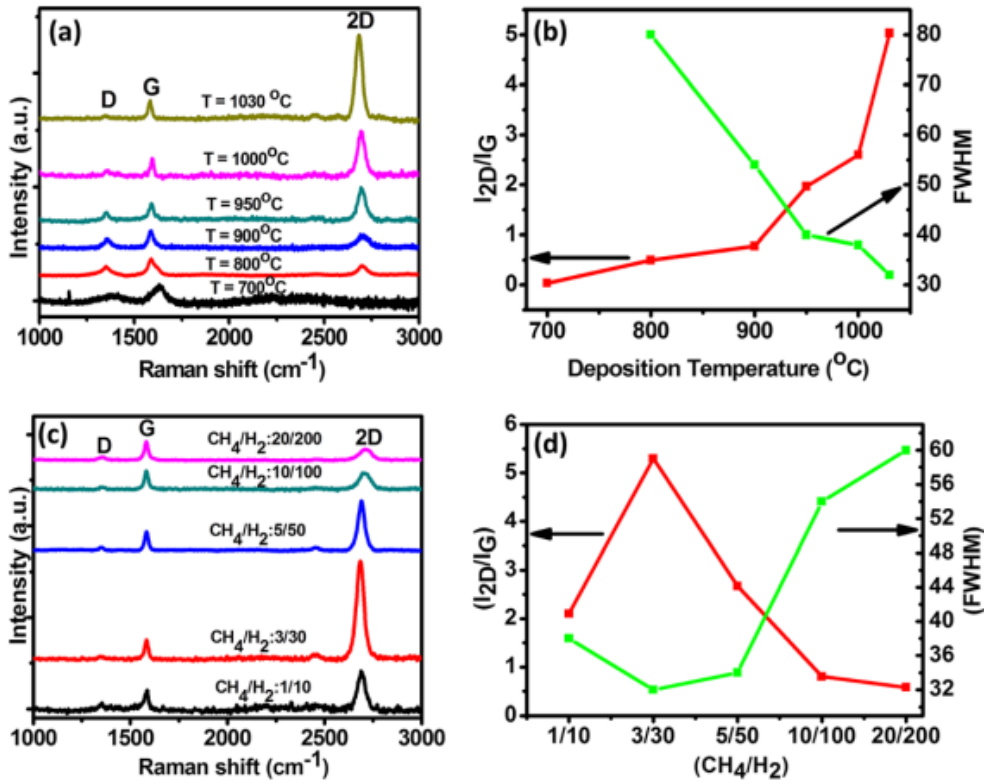

Figure 2. Raman spectra of graphene deposited onto copper via CVD at (a) different temperatures and (c) different gas flow rates, and (b, d) corresponding I_{2D}:I_G ratios and FWHM of 2D peaks of each spectrum, respectively (Kumar *et al.*, 2014).

In addition to Raman spectroscopy, an imaging technique known as scanning electron microscopy (SEM) was used for graphene characterisation in this work. SEM provides invaluable information such as nucleation density, sample coverage, grain size and morphology. SEM is mostly used to obtain an estimate of the uniformity of graphene layers, as it cannot be used to evaluate the exact number of graphene layers present. Although, the contrast in the images does provide information on where thicker (darker) and thinner (lighter) layers have been deposited. As uniform graphene thickness is more desirable, a uniform contrast in a SEM image is ideal. Additionally, defects such as voids, wrinkles and holes within the graphene can be visualised by SEM (Saeed *et al.*, 2020).

2 THE AIMS OF THE THESIS

There were three main goals to be achieved within this thesis work. These goals may also be described in the form of three different experiments with their specific aims. All the experiments were, essentially, devoted to the synthesis, analysis, and application possibilities of graphene in the Laboratory of Thin Film Technology at the Institute of Physics of University of Tartu. The main hypothesis behind the research work was related to the expectation that uniform graphene layers, synthesized in the same laboratory, will retain their integrity upon transfer procedures, heat-treatments, and plasma-assisted deposition of other materials' layers on the surface of graphene, necessary before construction of functional devises containing graphene layers.

The experiments with their aims can be described in more detail as follows:

1. The aim of the first experiment was to see whether graphene would be of higher quality on hydrophilic substrates, as it should be easier to transfer graphene onto, compared to hydrophobic substrates. The ease of transfer could thus result in less wrinkled and defective graphene. Also, the aim was to see whether different substrate cleaning methods contribute to the graphene quality.
2. The aim of the second experiment was to see whether amorphous carbon would absorb into a carbon diffusion layer, nickel, upon annealing and crystallize into graphene outside of nickel after cooling. Secondly, the aim is to see whether prior to annealing, nickel could absorb enough carbon from its surroundings so that graphene could form without an additional carbon source, such as amorphous carbon. Lastly, the aim is to see whether graphene forms both on top and bottom of nickel and see whether a carbon diffusion barrier could stop graphene formation above the carbon diffusion layer and entice the graphene to form between the substrate and nickel.
3. The aim of the third experiment was to see whether graphene could be transferred between SiO_2 and HfO_2 oxide films without destroying its structure and, if not, to assess how much damage would be done to the graphene structure. Finally, the aim would be to evaluate the effect of using graphene on the properties of the resulting functional resistive switching devices.

3 EXPERIMENTAL PART

In the experiments described in this section, the following chemicals were used:

- Acetone (>99.5%, Honeywell),
- IPA (>99.5%, Honeywell),
- Acetic acid (99.8-100.5%, Sigma-Aldrich),
- PMMA (M_w ~996000, Sigma-Aldrich),
- Ammonium persulfate (>98%, Sigma-Aldrich),
- Iron (III) chloride (98%, Strem Chemicals),
- Chlorobenzene (99%, Alfa Aesar),
- Dichloromethane (>99.8%, Sigma-Aldrich),
- Deionized (DI) water,
- Hydrogen peroxide (>35%, Carl Roth) used in the RCA substrate cleaning method,
- Ammonium hydroxide (28-30%, Sigma-Aldrich) used in the RCA substrate cleaning method,
- Hydrochloric acid (>37%, Sigma-Aldrich) used in the RCA substrate cleaning method.

To characterize the quality and analyse the properties of the graphene and thin films obtained in the experiments of this section, the following techniques were used:

- **XRR** analyses of the thickness, density and roughness of the obtained films were done with a SmartLab Rigaku diffractometer.
- **SEM** analyses of graphene were done with a high-resolution scanning electron microscope (Helios NanoLab^{TM} 600, FEI).
- **Raman** analyses of graphene were done with a Raman spectrometer (inVia micro-Raman spectrometer, Renishaw). All graphene-containing devices were measured with a laser of 514 nm wavelength and at 10%, 50% or 100% laser power, depending on the intensity of the background interference. The Raman spectra were measured at 1200 to 3300 cm^{-1} intervals. All stacked Raman spectra in this work are normalized by the G-band.
- **Electrical characterization** using a light-proof and electrically shielded box with Cascade Microtech MPS150 probe station, Keithley 2636A source-meter.

The following gas flow rates were used whenever the CVD reactor was utilized: 50 sccm of Ar, 10 sccm of H_2, 30 sccm of Ar/CH_4 (10%).

3.1 METHODS

3.1.1 Graphene deposition on metal catalysts and its wet chemical transfer

This method was based off the technique of growing monolayer graphene on a copper foil and subsequently transferring the graphene onto an appropriate substrate (Kalita, 2015).

For the growth of graphene, a polycrystalline copper foil was used as a metal catalyst. To ensure the growth of high-quality graphene on the Cu foil, the foil must be as flat as possible. The flat foil was first placed in an ultrasonic bath with acetone for 5 minutes to remove any organic residues and was then placed in the ultrasonic bath with DI water for another 5 minutes to remove residual acetone. To remove any copper oxide, the foil was left in 20% acetic acid for 10 minutes and later rinsed with DI water and IPA.

Monolayer graphene was grown on the Cu foil in an in-house built hot-wall type CVD reactor in low pressure conditions of 1.5×10^{-2} mbar. The foil was annealed at 1000 $^{\circ}$C in Ar and H_2 gas flow for 1 hour, after which the graphene deposition commenced with Ar/CH_4 (10%) being turned on for 2 hours.

Wet chemical transfer was used, where a polymer layer, in this case PMMA, is spin-coated onto the graphene, the underlying Cu foil is etched away and the graphene is transferred onto the desired substrate (Li *et al.*, 2009). To influence the adhesion properties of graphene, the wettability of the substrates was altered by plasma treatment (Lukose *et al.*, 2021).

PMMA was dissolved in dichloromethane and used to coat one side of the graphene-covered Cu foil with the help of a spin coater. The unprotected graphene side was etched with Ar^+ ions for 6 minutes in a plasma system (Femto low pressure plasma system, Diener Electronic). The Cu-G-PMMA was cut into ca. 5 by 5 mm pieces and were left overnight in 0.1 M ammonium persulfate solution to etch the copper. Upon completion of the etching process, the graphene pieces were gently cleaned by moving them multiple times from one DI water bath to another.

P-type, boron-doped 10 by 10 mm silicon wafers with 300 nm thick SiO_2 were used as substrates for the graphene. Two substrate pieces were preliminarily cleaned by removal of organics with a piranha solution, then cleaned with the Radio Corporation of America (RCA) cleaning method (Kern, 1990). Two other pieces of substrate were cleaned by leaving them in boiling acetone for 10 minutes.

A single substrate from each cleaning method was plasma-treated for 1 min with Ar^+ ions at 30% power to make them hydrophilic and achieve more uniform spreading of graphene upon transfer. The PMMA-covered graphene pieces were transferred onto each of these substrates, as well as two equivalent hydrophobic substrates without the plasma treatment. The transferring was done by submerging the substrates in the water with floating graphene and carefully scooping it up while making sure it had stuck to the centre of the substrate.

Finally, the dry Si-SiO_2-G-PMMA devices were heat-treated at 100 °C on a hot plate to improve contact between the substrate and graphene. This step was useful against any wrinkles or water bubbles that could have occurred between the graphene and substrate during the transfer process. The heat-treated devices were placed in dichloromethane for 1.5 hours to dissolve the PMMA and lastly rinsed with IPA.

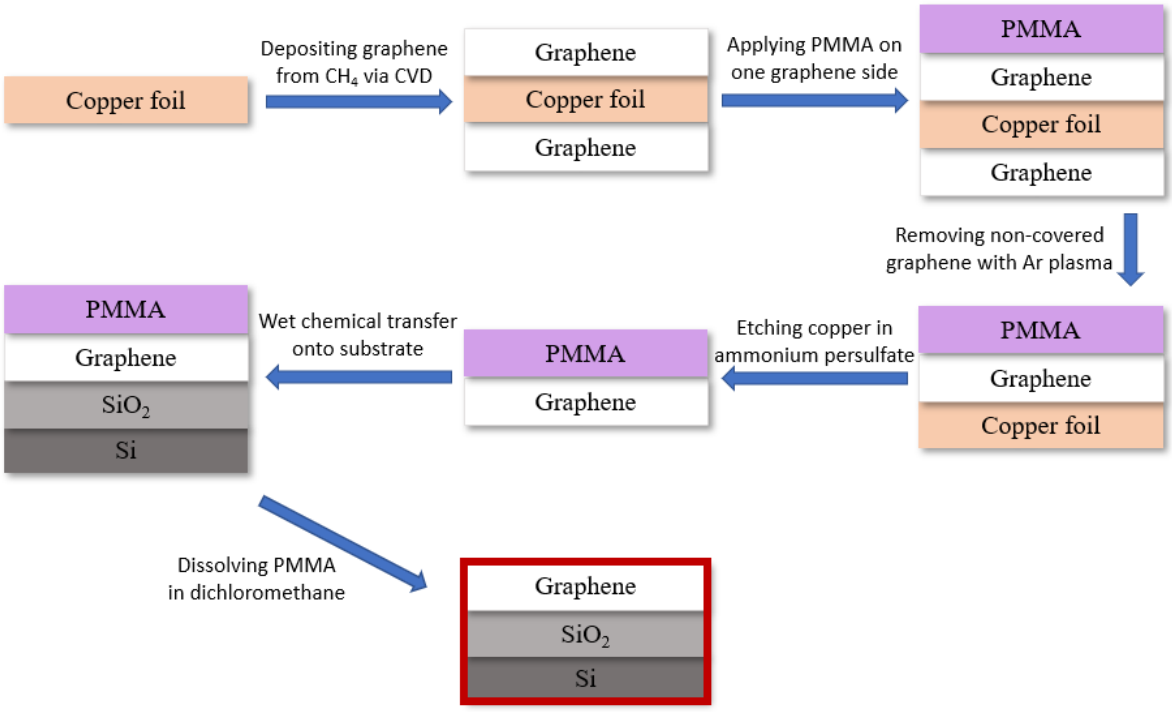

Figure 3. Simplified schematic of the process of transferring graphene onto a substrate, starting from a copper foil. The schematic does not include manipulations with the substrate, such as cleaning and plasma-treatment.

3.1.2 Directly-formed graphene from amorphous carbon with nickel catalyst

For this method, the idea was to form graphene directly on the desired substrate without the need to transfer it. By annealing a carbon source deposited onto the substrate, the carbon source would decompose and be dissolved into a carbon diffusion layer and upon cooling would form graphene on both sides of the carbon diffusion layer (Peng *et al.*, 2011; Vishwakarma *et al.*,

2017). Additionally, a carbon diffusion barrier was applied on some of the devices to see whether the formation of graphene could be limited to the interface of the substrate and carbon diffusion layer (Kim *et al.*, 2018). In this work, amorphous carbon acted as the carbon source, nickel as the carbon diffusion layer and titanium as the carbon diffusion barrier.

A boron-doped silicon wafer covered with 300 nm thick SiO_2 was used to cut out three substrate pieces. An amorphous carbon (aC) film was evaporated onto one Si-SiO_2 substrate with the use of Ar^+ ions in electron beam evaporation (EBE). A metal catalyst layer of nickel was also evaporated via EBE onto the substrate with aC as well as on the analogous ones without it. All aC and Ni films were deposited by Dr. Aarne Kasikov. The resulting devices were: one Si-SiO_2-aC-Ni and two Si-SiO_2-Ni devices.

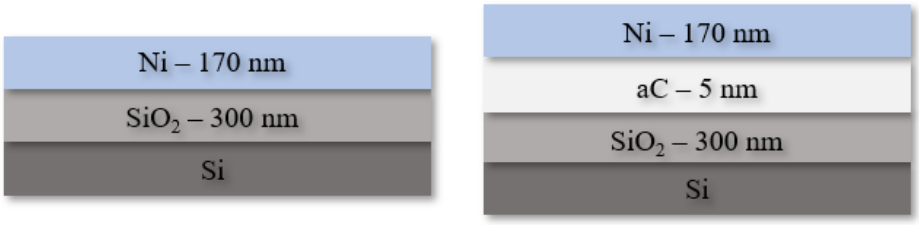

Figure 4. Schematics of the two types of devices designed for further experiments. The thickness of the films is nominal.

One device of each type was annealed for 30 minutes at 1000 ˚C in a CVD reactor chamber. The annealing occurred in Ar and H_2 gas flow and a low-pressure environment of 1.5×10^{-2} mbar. At the end of the annealing, the heater was moved away from the devices to induce fast cooling. Leaving the Ar gas flowing, the H_2 gas was turned off when the reactor temperature had dropped to 300 ˚C. The second Si-SiO_2-Ni device was left as a reference.

The annealed aC-Ni device was cut into smaller pieces. The top film of one such piece was etched by plasma for 10 minutes at 100% power with the use of Ar^+ ion plasma. The nickel was then etched by a 0.5M solution of iron (III) chloride from all devices. The devices were left in solution for 11 minutes and then carefully rinsed with DI water. The results were analysed.

In addition to this, experiments were done on similar aC and Ni containing devices with an additional carbon diffusion barrier in the form of a titanium film (Figure 5). TiN-covered Si wafers were used as substrates in these devices. The Si wafers with a resistivity of 0.014–0.020 Ω·cm were pre-covered by 10 nm thick nanocrystalline titanium nitride (TiN) electrode layers. The commercial Si wafers were boron-doped to concentrations ranging from 5×10^{18} to 1×10^{19} cm^{-3} and the TiN layer was pre-grown by pulsed chemical vapor deposition using a batch

$TiCl_4/NH_3$ process (Granneman *et al.*, 2007; Zagwijn *et al.*, 2008) at temperatures of 450 to 500 °C in an ASM A412 Large Batch 300 mm reactor at Fraunhofer IPMS-CNT. The SiO_2 was grown via atomic layer deposition (ALD) in an in-house built flow-type hot-wall ALD reactor, schematically described in a study by Arroval *et al.* (Arroval *et al.*, 2016), with the use of hexakis(ethylamino)disilane, i.e. $Si_2(NHC_2H_5)_6$ and ozone, O_3, precursors at 240 ˚C (Matero *et al.*, 2008; Kukli *et al.*, 2020),. The depositions were carried out by Dr. Taivo Jõgiaas. 75 ALD cycles were done with pulse and purge time sequences of 2–2–5–5 seconds for $Si_2(NHC_2H_5)_6$ pulse-purge-O_3 pulse-purge lengths, respectively. Furthermore, the aC, Ni and Ti films were deposited onto the device via EBE by Dr. Aarne Kasikov.

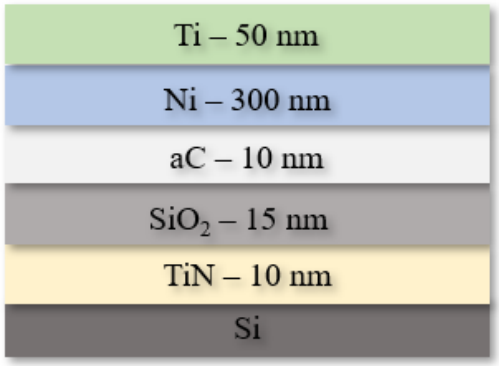

Figure 5. Schematics of the two identical devices used for further experiments. The thickness of the films above TiN is nominal.

As with the previous devices, these were also annealed but with the use of two different methods. The first device was annealed for 10 minutes in Ar and H_2 gas flow in a CVD reactor at 600 ˚C and 1 mbar pressure. The second device was annealed for 10 minutes in the high-vacuum chamber at 600 ˚C and lower pressure of 10^{-5} to 10^{-6} mbar. Afterwards the devices were etched in 0.5M iron (III) chloride for 20 minutes and the results analysed.

3.1.3 Graphene with insulator dielectrics for resistive switching devices

TiN-covered Si wafers, described in detail in the last section (3.2.2), were used as a base stack for deposition of SiO_2 and HfO_2 dielectric films. Reference stacks of insulator dielectrics were grown by depositing SiO_2 directly onto TiN, followed by the deposition of HfO_2 on SiO_2 (Figure 6 A). Additionally, one of such devices was annealed at 1000 ˚C for 10 minutes prior to growth of HfO_2 (Figure 6 C). The SiO_2 films were grown by the same method as described for the aC-Ni-Ti device in the previous section. The HfO_2 films were grown from hafnium tetrakis(ethylmethylamide), i.e. $Hf[N(CH_3)(C_2H_5)]_4$, also denoted as TEMAH, and O_2 plasma in a commercial Picosun R-200 Advanced ALD system. The depositions were carried out by

Mr. Aivar Tarre at 240 °C. The amount of ALD cycles was 80 with pulse/purge time sequences of 0.3–4–15–4 seconds for TEMAH pulse-purge-O_2 plasma pulse-purge lengths, respectively.

It is worth mentioning that the SiO_2 and HfO_2 films grown in this method, as well as the SiO_2 film in the aC-Ni-Ti device from the previous section, most likely have vacancy rich oxide but will be denoted as dioxide for ease of reading.

To build stacks containing graphene layers, graphene was transferred to the SiO_2 film using the same method as described in section 3.2.1, and then covered by the ALD-grown HfO_2 film (Figure 6 B and D), exploiting a procedure analogous to that used and described earlier by Kahro *et al*. (Kahro *et al.*, 2021).

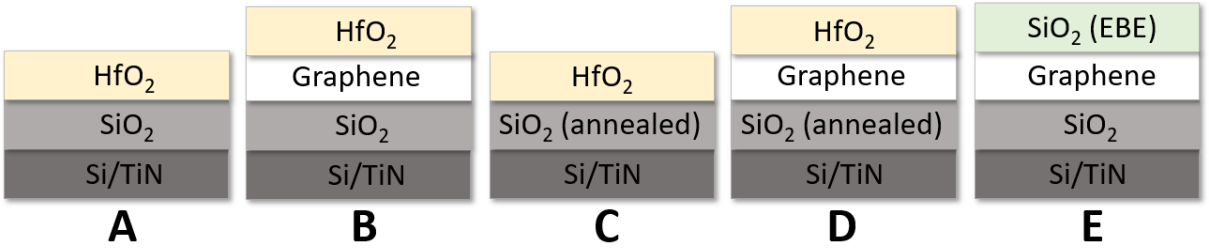

Figure 6. Schematic representation of substrate and thin film stacks designed for the electrical measurements. For the explanation of labels, see the text referring to the figure.

To examine possible effects of post-deposition thermal treatments to the device performance, selected Si-TiN-SiO_2 (Figure 6 C and D) were, prior to further depositions, rather aggressively annealed in Ar flow at 1000 °C for 10 minutes. The increment in temperature from 500 °C to 1000 °C was 13.7 deg/min and cooling duration down to 500 °C was 30 minutes (see Appendix).

Finally, Si-TiN-SiO_2-graphene-SiO_2 stack (Figure 6 E) was prepared, where the first SiO_2 layer was grown by ALD onto TiN, then the graphene layer was transferred onto the surface of the SiO_2 film, and the graphene was covered by an SiO_2 film made with EBE. The evaporation was carried out by Dr. Aarne Kasikov.

To create functional and measurable resistive switching cells (Celano, 2016; Ye *et al.*, 2016; Slesazeck and Mikolajick, 2019; Banerjee *et al.*, 2020), top electrodes of titanium metal (Ti) were prepared on the surface of HfO_2 film using maskless photolithography in the cleanroom facility at the Institute of Physics. The diameters of dot electrodes in the matrix were 50 and 250 μm.

3.2 RESULTS

3.2.1 Graphene on hydrophobic and hydrophilic substrates

In the first experiment described in paragraph 3.2.1, the resulting devices were the following: Si-SiO_2-G with a hydrophobic substrate cleaned with the RCA method, as well as Si-SiO_2-G with a hydrophobic substrate cleaned with boiling acetone and its plasma-treated hydrophilic equivalent. Due to an error explained in section 3.4.1, the transferring of graphene onto RCA-cleaned hydrophilic substrate had failed and will not be analysed.

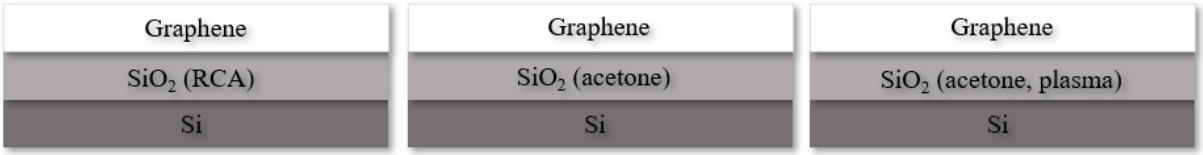

Figure 7. Schematic of the obtained devices used for further measurements. Substrate cleaned by the RCA method is denoted as 'RCA', and the substrate cleaned in boiling acetone is denoted as 'acetone'. Plasma-treated substrate is denoted as 'plasma'.

The following figure depicts the SEM images of graphene transferred onto hydrophobic substrates with different substrate cleaning methods. Visually, one could say that the RCA method, depicted on the left, is more effective at eliminating impurities from the substrate.

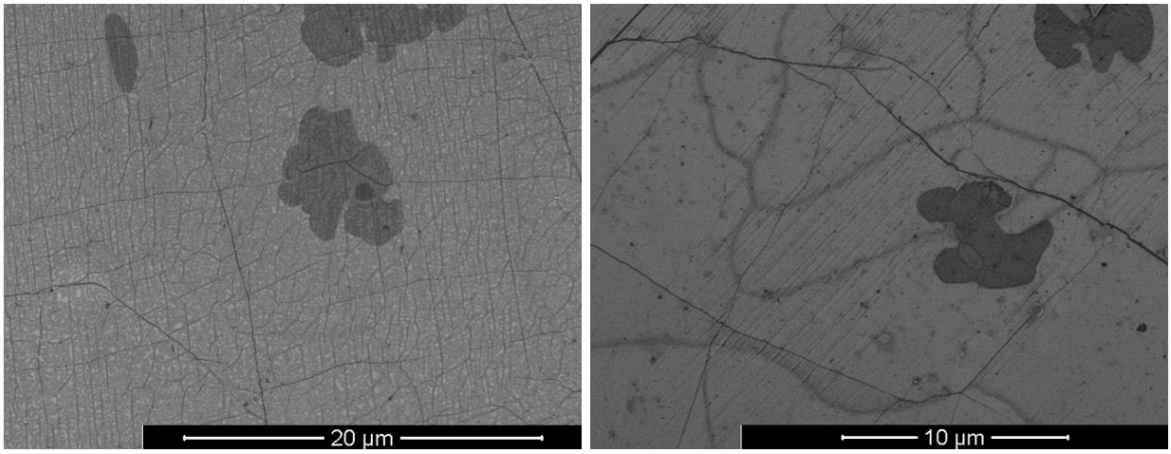

Figure 8. SEM images of graphene transferred onto hydrophobic RCA-cleaned (left) and boiling-acetone-cleaned (right) substrates. Lighter grey is monolayer and darker grey is bilayer graphene.

Raman spectra were measured to further analyse the effects of graphene on hydrophilic and hydrophobic substrates as well as the different substrate cleaning methods on the quality of graphene. Figure 9 depicts the differences in the 2D-bands of monolayer graphene in each of

the device types. The graphene on a hydrophobic acetone-cleaned device (Figure 9 B) has Raman shift values of approximately 2688 cm^{-1}. As expected from graphene on a hydrophilic substrate (Figure 9 C), its 2D peak shifted to slightly higher Raman shift values of approximately 2696 cm^{-1}. The 2D peak Raman shift values of the hydrophobic RCA-cleaned device are ca. 2694 cm^{-1} (Figure 9 A). Despite the impurities visible on the SEM image of the acetone-cleaned device, there are no apparent D bands on any of the Raman spectra.

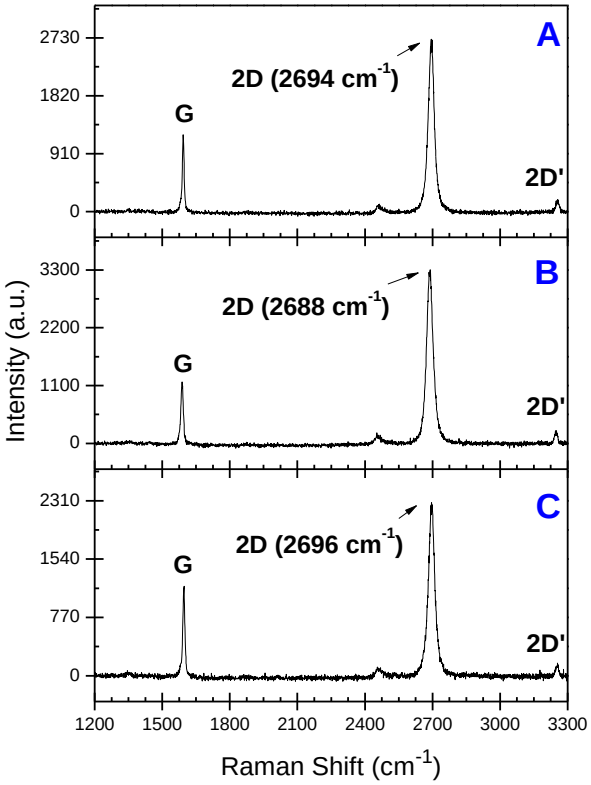

Figure 9. Raman spectra of graphene transferred onto A) hydrophobic RCA-cleaned substrate, B) hydrophobic acetone-cleaned substrate, and C) hydrophilic acetone-cleaned substrate.

3.2.2 Graphene directly formed from amorphous carbon

Figure 10 shows optical microscope images of the two types of devices, as described in section 3.2.2, after annealing and prior to etching of nickel. The top layer of Si-SiO_2-Ni on the left looks to be crystallized nickel, while the Si-SiO_2-aC-Ni on the right has light and dark islands resembling graphene on the nickel.

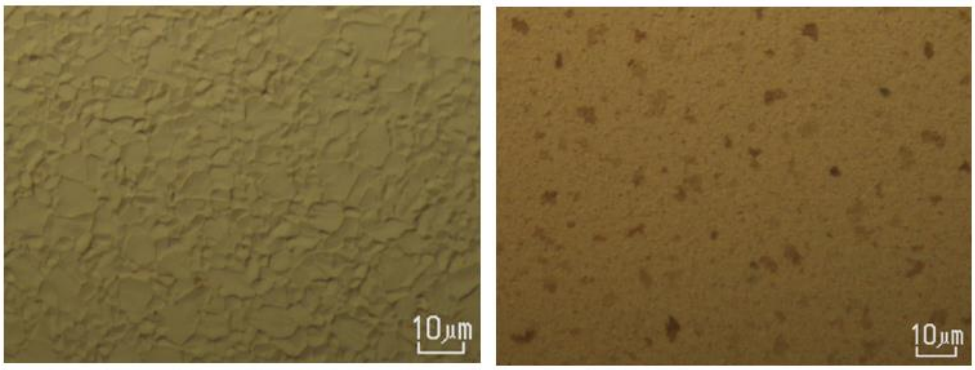

Figure 10. Optical microscope images of annealed Si-SiO_2-Ni (left) and Si-SiO_2-aC-Ni (right). Nickel surface is seemingly crystallised on the Si-SiO_2-Ni; some light and dark islands are present on the Si-SiO_2-aC-Ni.

In addition, the SEM images of the annealed aC-Ni device resembled typical multilayer graphene with lighter and darker islands corresponding to graphene of different thickness.

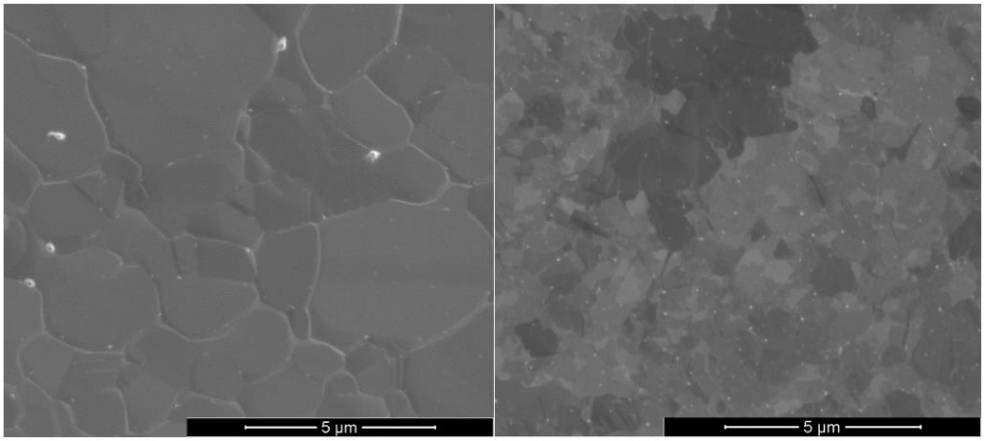

Figure 11. SEM images of the Si-SiO_2-Ni device on the left and the Si-SiO_2-aC-Ni device on the right. The former is seemingly crystallized nickel, while the latter resembles graphene islands.

Raman spectroscopy confirmed that no graphene had formed on the Si-SiO_2-Ni device. As seen on the following figure there are no evident 2D nor G peaks typically seen for a graphene device.

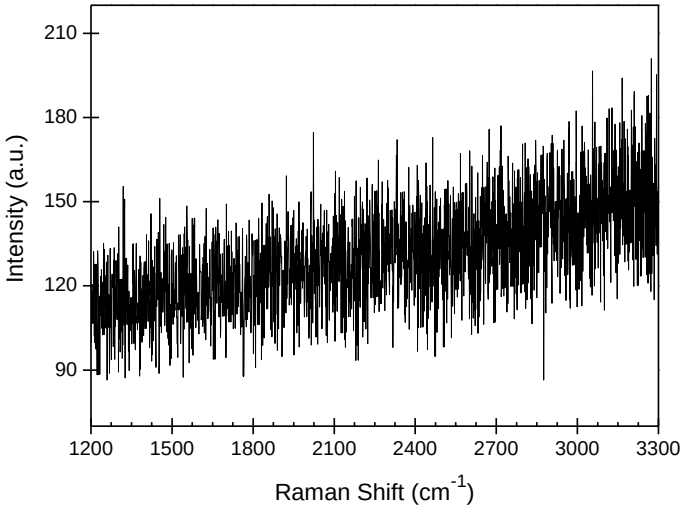

Figure 12. Raman spectrum of Si-SiO_2-Ni. No peaks characteristic to graphene are present.

In contrast, the graphene in the aC-Ni device spectra had visible 2D and G peaks. The optical microscope image on the right side of Figure 13 suggests that the graphene on the aC-Ni device is not a monolayer, but rather contains multilayer islands. As seen on the Raman spectra in the same figure, the wide and splitting 2D peaks as well as the difference between G and 2D peak intensities (I_{2D}:$I_G \leq 0.58$), show that the graphene is multilayer (Nguyen *et al.*, 2013). The minor presence of the D peak suggests that the graphene has defects such as holes.

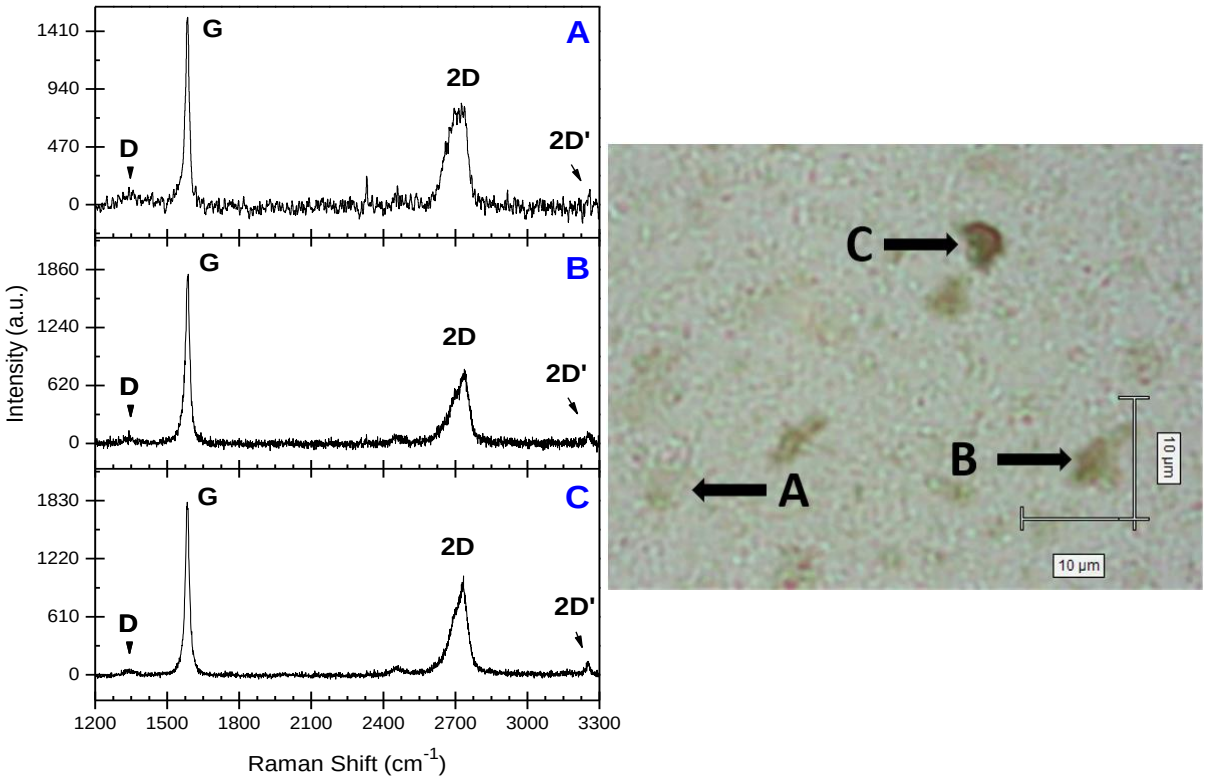

Figure 13. Raman spectra and optical microscope image of Si-SiO_2-aC-Ni. A, B and C represent lighter to darker graphene islands, respectively.

The optical microscope images in Figure 14 were obtained after annealing of one aC-Ni device and after the annealing and plasma-etching of a second aC-Ni device. The non-etched device has islands of different colour intensity and resembles the graphene islands in Figure 10 (right). The device with plasma etching has a uniform layer which does not resemble the previously seen images with graphene islands, thus the top graphene layer was completely etched away.

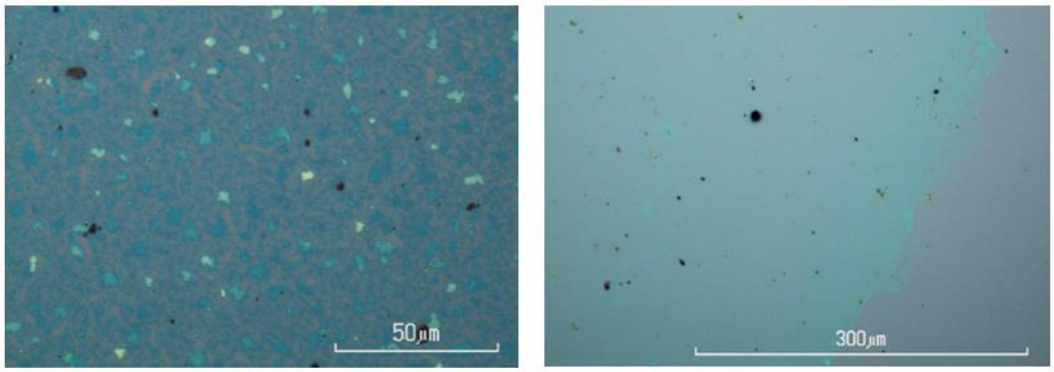

Figure 14. Optical microscope images of annealed (left) and annealed and plasma-etched (right) Si-SiO_2-aC-Ni. The surface of the device without plasma etching resembles graphene islands. The surface of the plasma-etched device resembles a uniform layer absent of graphene islands.

Figure 15 and Figure 16 show the Raman spectra of the aC-Ni devices where no plasma etching of the top graphene layer was done and the spectra of the device where the top graphene was etched by plasma, respectively, after etching of nickel. As seen, the device without plasma etching still has graphene present, although the coverage is low (<5% of the substrate). Due to the high intensity of the D peak and the presence of the D+D' peak, the graphene appears to be of quite low quality and by the looks of the optical image, there seems to be residual nickel present too. After visual estimation one may suppose that the brighter blue is thicker multilayer graphene. The slight shift to higher Raman shift values of the B spectra (~2698 cm^{-1}) compared to spectra A (~2691 cm^{-1}) could also suggest that the former is thicker graphene, but further studies of the spectra must be done to confirm this.

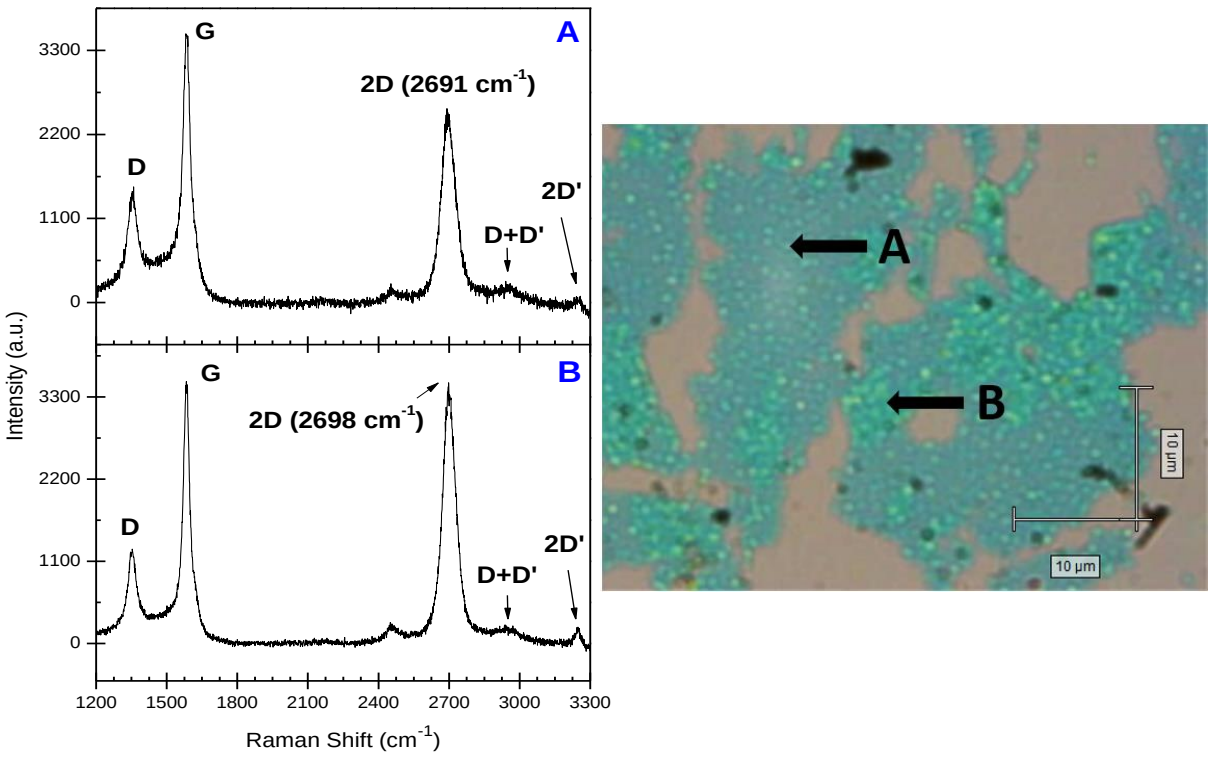

Figure 15. Optical microscope image of non-plasma-treated Si-SiO_2-aC-Ni and its Raman spectra. A and B correspond to graphene of different thickness. This optical image is of one of the few areas with graphene coverage.

In contrast to the device which did not undergo plasma etching, the device which did has no characteristic 2D peak and, while the G peak is present, the layer under nickel seems to be mostly amorphous carbon rather than graphene.

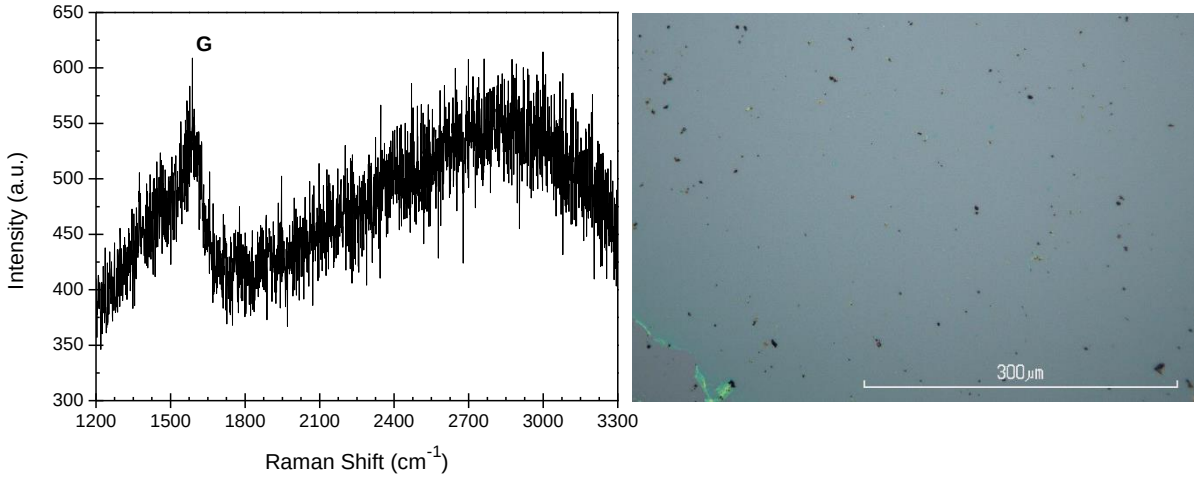

Figure 16. Raman spectrum of plasma-treated Si-SiO_2-aC-Ni and its optical microscope image. 2D peak characteristic to graphene is absent, but G peak is present suggesting that the layer under nickel was amorphous carbon.

In addition to the aC-Ni and plain Ni devices, devices containing a top Ti layer were analysed. The two Si-TiN-SiO_2-aC-Ni-Ti devices demonstrated very different optical images after annealing in different conditions. As seen from the top images of Figure 17, the device annealed in high vacuum had a smooth surface, while the one annealed in low vacuum had a bubbly surface. The bottom of the figure shows the same devices after the etching process. While the device annealed at lower pressure had no graphene at all, the device annealed at relatively higher pressure did have graphene formed on the SiO_2. The bubbles in the latter were holes without graphene.

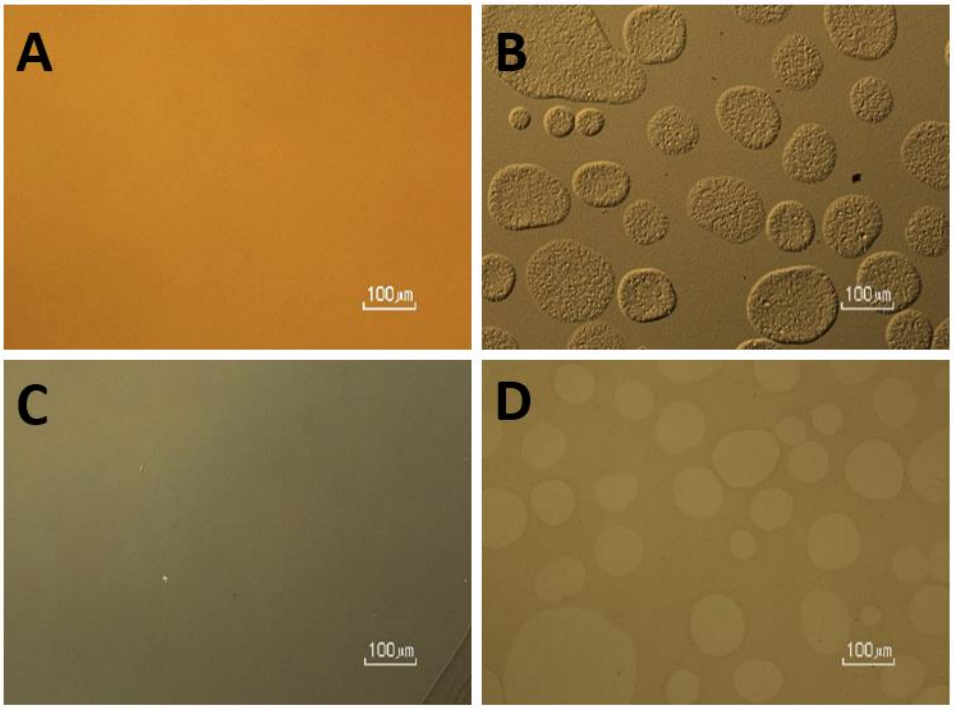

Figure 17. Optical microscope images of Si-TiN-SiO_2-aC-Ni-Ti devices where A) was annealed in high vacuum, B) was annealed in low vacuum, while C) and D) are their equivalents after nickel etching.

The quality of the graphene in the aC-Ni-Ti device annealed in low vacuum can be seen in the SEM image of Figure 18 as well as its Raman spectrum. The graphene in the SEM image is grainy, non-uniform and seemingly varies in thickness. The Raman spectrum shows a low-intensity 2D peak and a comparatively high-intensity D peak, confirming the poor graphene quality. The sharp line in the middle denoted as N_2 comes from the TiN layer in the base stack. As seen best around D and G peaks, at lower Raman shift values the background noise of the substrate is high.

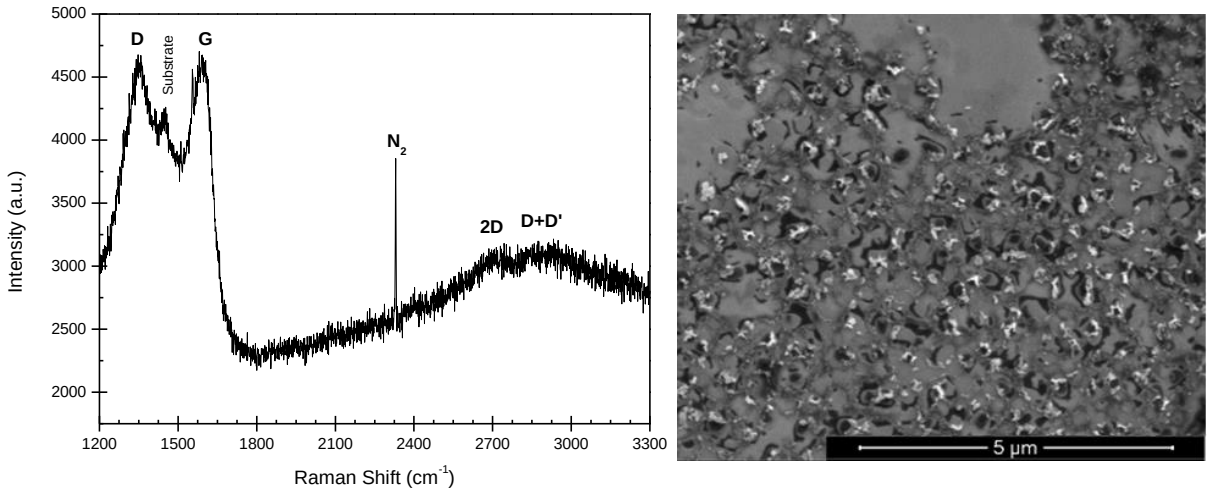

Figure 18. SEM image of the Si-TiN-SiO_2-aC-Ni-Ti device and its Raman spectrum.

3.2.3 Resistive switching devices

Raman spectra of the devices after transferring graphene onto the non-annealed and annealed base stacks and prior to depositing the next oxide layer (Figure 20), as well as after depositing the oxide layers on the transferred graphene (Figure 21), were measured. The structural integrity of the graphene was analysed with the use of these spectra, as well as SEM images of the non-annealed and annealed devices prior to the deposition of an oxide layer onto the transferred graphene seen in Figure 19.

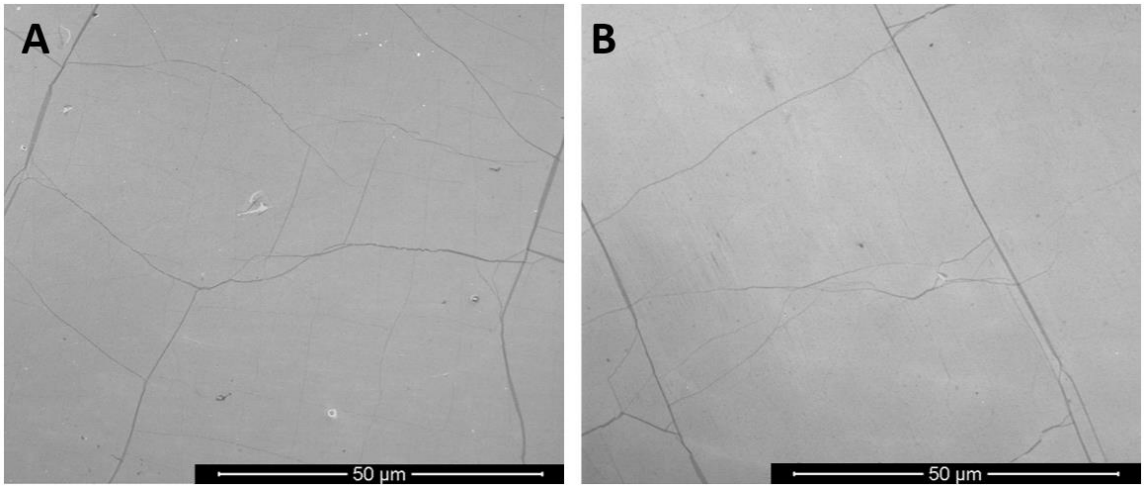

Figure 19. SEM images of the cell structures of A) graphene on non-annealed Si-TiN-SiO_2, and B) graphene on annealed Si-TiN-SiO_2 devices.

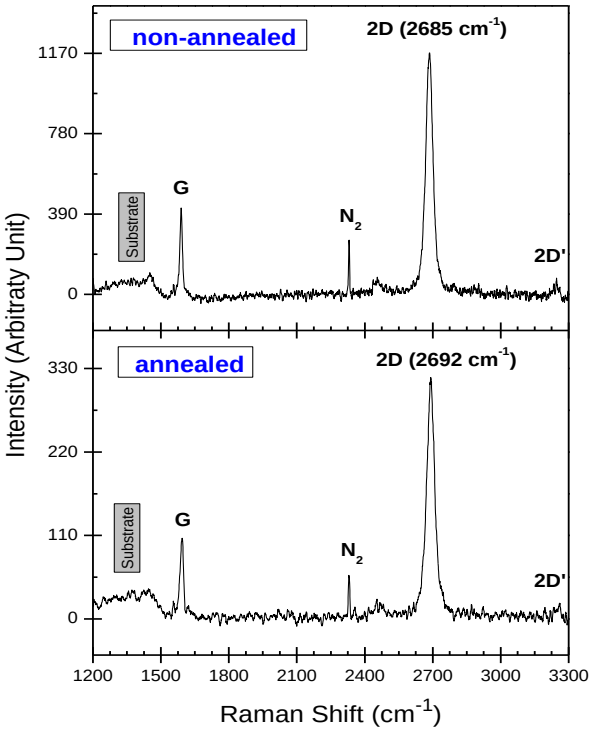

Figure 20. Raman spectra of the Si-TiN-SiO_2-graphene cell structure, where the Si-TiN-SiO_2 base stack was A) not annealed and B) annealed at 1000 °C.

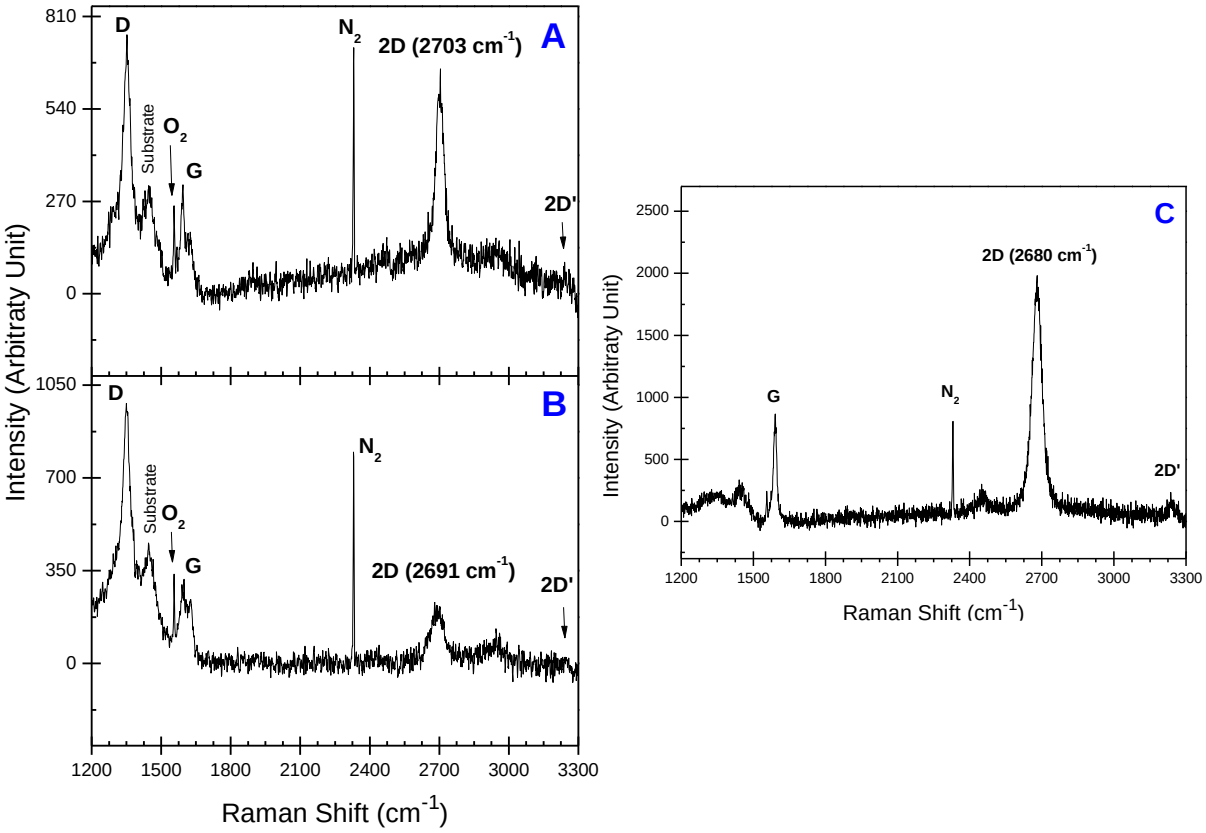

Figure 21. Raman spectra of A) the non-annealed Si-TiN-SiO_2-graphene-HfO_2, B) the annealed Si-TiN-SiO_2-graphene-HfO_2, and C) the non-annealed Si-TiN-SiO_2-graphene-SiO_2 where the bottom SiO_2 layer was made by ALD and the top made by EBE.

The thickness, density, and roughness of the SiO_2 layer on TiN, before and after annealing (Figure 6 C and D), was evaluated by X-ray reflectivity (XRR) measurements. The structure with as-deposited SiO_2 could quite conveniently be modelled (Figure 22 (a)). Further, one could see, that, upon annealing, the layer thickness was decreased from 7.9 to 4.3 nm, and density was increased from 1.76 to 2.77 g/cm^3 (Figure 22 (b)). Notably, surface roughness was quite insignificantly increased from 0.60 to 0.63 nm. Based on the XRR results, one might conclude that the SiO_2 layer was noticeably densified under annealing conditions. Somewhat expectedly, the interface between SiO_2 and TiN was chemically changed, as the TiN layer must have been partially oxidized. The latter was revealed after apparent necessity to consider nearly 2 nm thick interfacial TiO_2 layer in the fitting model applied in the XRR measurements.

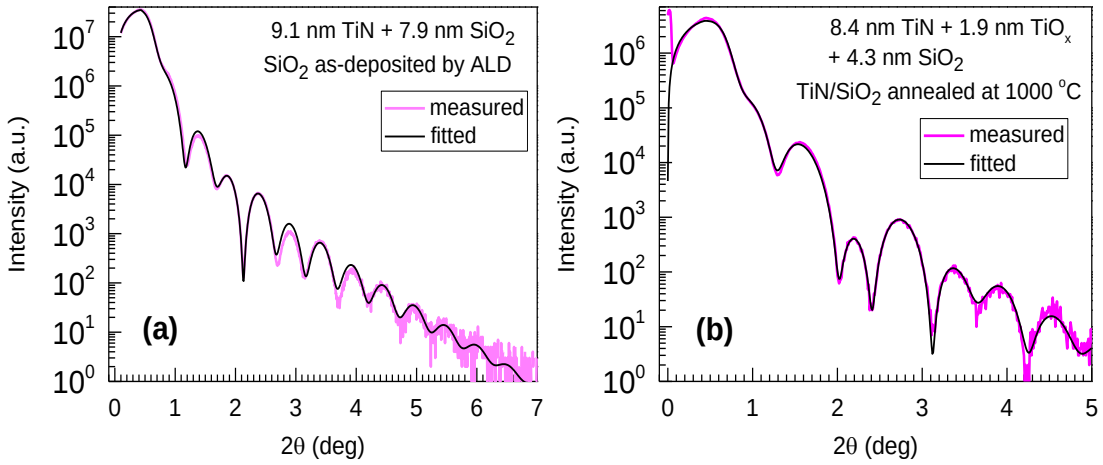

Figure 22. Measured and model fitted X-ray reflectivity curves from as-deposited (a), and annealed (b) Si-TiN-SiO_2 stacks.

Electrical measurements were carried out by Mr. Joonas Merisalu using a light-proof and electrically shielded box with Cascade Microtech MPS150 probe station, Keithley 2636A source-meter.

The Si-TiN-SiO_2-HfO_2-Ti devices did not switch resistively (Figure 23). The cells stood against electrical fields of 20-25 MV/cm. The applied voltage could be varied in both polarity directions between 0 and as high as 40-50 V without evidence of reversible or irreversible breakdown events.

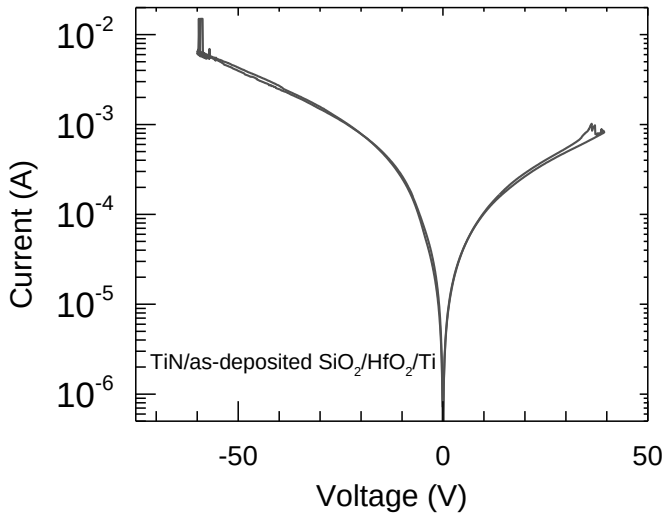

Figure 23. Current-voltage characteristics of Si-TiN-SiO_2-HfO_2-Ti cell structure. The diameter of top Ti electrode was 250 µm.

Figure 24 depicts signs of resistive switching recorded from the device containing as-deposited SiO_2. Although the currents were still in the order of 1-10 pA at voltages ranging from -1.5 to 1.5 V, where measurements are affected by charging-related noise, SET events started to occur in the voltage range of 2.0 to 4.5 V. The difference between low and high resistivity states (LRS and HRS, respectively) could extend over 4 orders of magnitude (I_{LRS}:I_{HRS} = 4600, on average). Although switching was not uniformly reproducible, the behaviour hints to possible performance. The switching type could be described as bipolar, meaning both SET and RESET events took place at different voltage polarities.

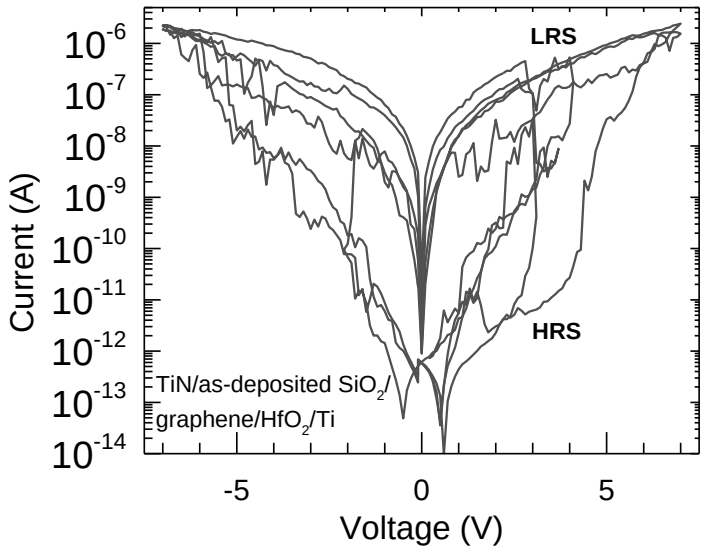

Figure 24. Current-voltage characteristics measured in resistive switching regime on the cell structure of Si-TiN-SiO_2-graphene-HfO_2-Ti, built on non-annealed Si-TiN-SiO_2 base stack.

The performance of Si-TiN-SiO_2-graphene-HfO_2-Ti devices (Figure 25) built on annealed SiO_2 layer was further improved in the sense of switching uniformity, compared to the devices containing as-deposited SiO_2 film. Although the LRS:HRS ratios (I_{LRS}:I_{HRS}) did not exceed 3-4, the repeatability of the switching cycles exceeded 500 (Figure 26).

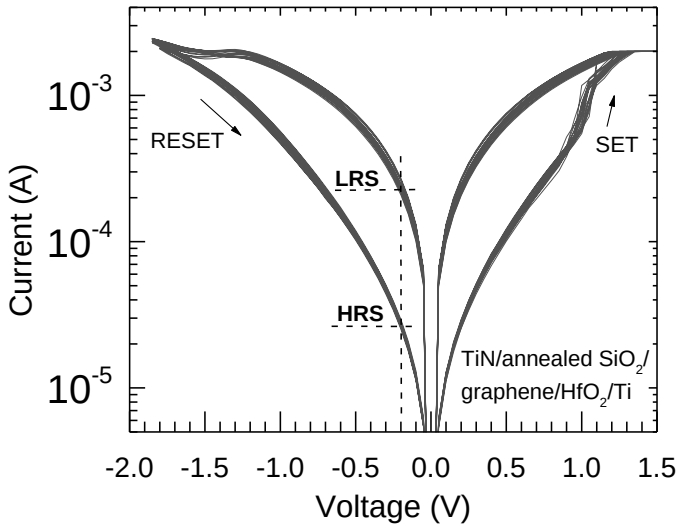

Figure 25. Current-voltage characteristics measured in resistive switching regime on cell structure of Si-TiN-SiO_2-graphene-HfO_2-Ti, built on Si-TiN-SiO_2 base stack annealed at 1000 °C. The LRS and HRS states, were further registered at programming voltages of 0.2 V.

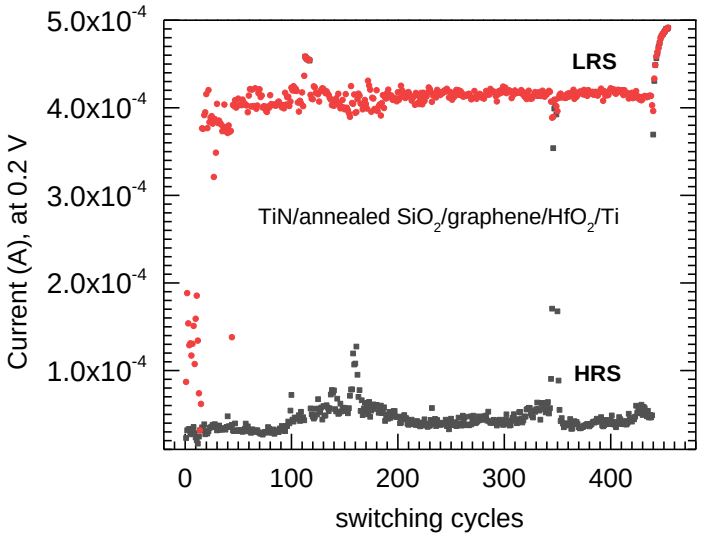

Figure 26. Endurance test characteristics measured on Si-TiN-SiO_2-graphene-HfO_2-Ti cell structure, built on Si-TiN-SiO_2 base stack annealed at 1000 °C. The LRS and HRS were recorded at voltages of 0.2 V.

Reference measurements were performed on Si-TiN-SiO_2-HfO_2-Ti cell structure, built on Si-TiN-SiO_2 base stack annealed at 1000 °C, not containing intermediate graphene layers. The

switching current-voltage curves could repeatedly be recorded (Figure 27). Figure 28 represents results of an endurance test carried out on a sample cell.

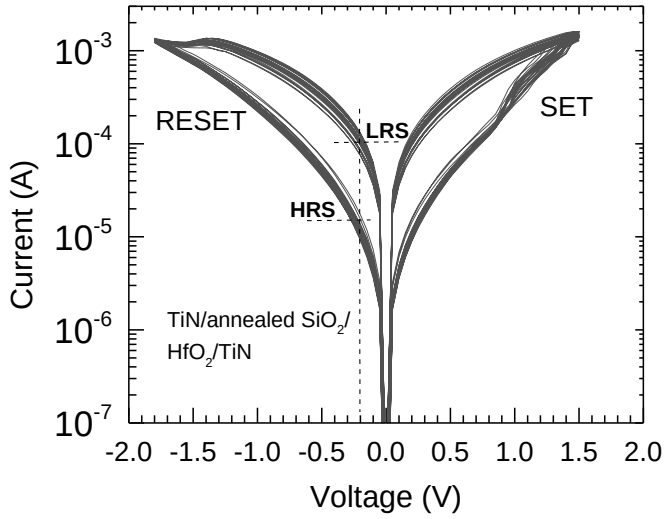

Figure 27. Current-voltage characteristics measured in resistive switching regime on the cell structure of Si-TiN-SiO_2-HfO_2-Ti, built on Si-TiN-SiO_2 base stack annealed at 1000 °C.

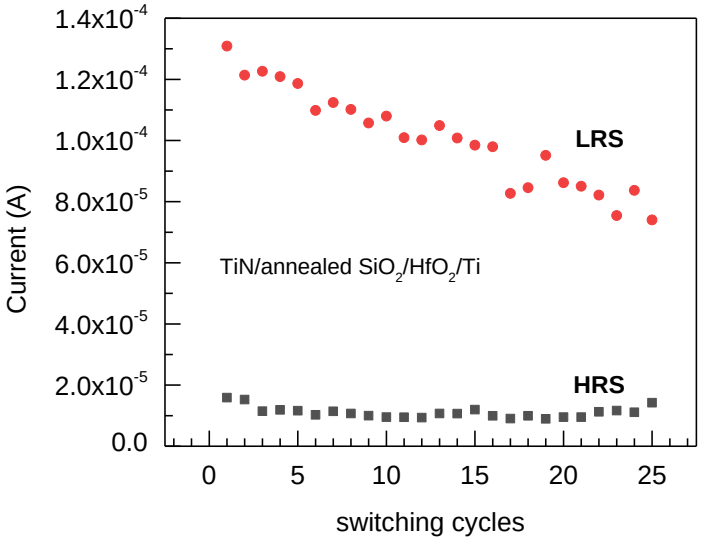

Figure 28. Endurance test characteristics measured on Si-TiN-SiO_2-HfO_2-Ti cell structure, built on Si-TiN-SiO_2 base stack annealed at 1000 °C. The LRS and HRS were recorded at voltages of 0.2 V.

The Si-TiN-SiO_2-graphene-SiO_2-Ti stack could also be instigated to act as a resistive switching cell (Figure 29), provided that the measurements were carried out in the light-shielded probe station. Remarkably, the SET events, i.e. the switching from high resistivity state to low resistivity state, took place at unexpectedly high voltages ranging from 15 to 30 V. Since the switching cycles were repeatable, together with the RESET events occurring between 10 and

15 V, the performance of the cell is to be regarded as that describing a resistive switching device, despite the remarkably high switching voltages and asymmetry in the current-voltage characteristics.

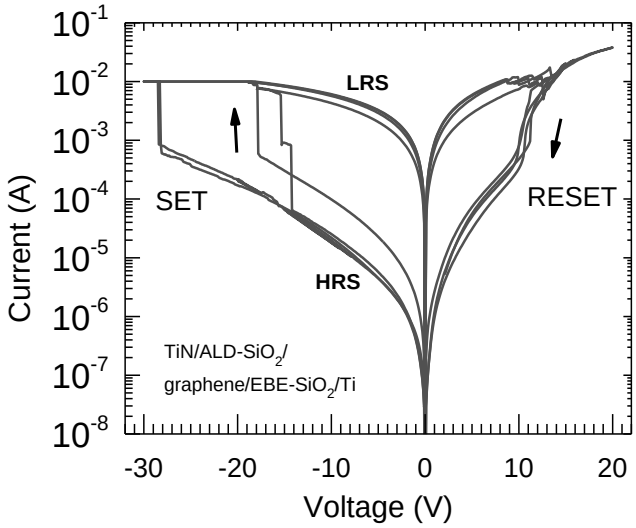

Figure 29. Measured current-voltage curves of resistively switching cell structure of Si-TiN-SiO_2-graphene-SiO_2-Ti devices.

3.3 DISCUSSION

3.3.1 Effect of substrate on the quality of transferred graphene

With regards to the failed attempt at transferring graphene onto the RCA-cleaned hydrophilic substrate, it can be said that neither the substrate cleaning method nor plasma-treatment is at fault for the failure of the initial transfer attempt. It is a possibility that water bubbles remained between the graphene and the substrate after transfer and the subsequent heat treatment on a hot plate had caused the water to evaporate by rupturing the graphene. Necessary measures were taken in the latter experiments to ensure that water would not become trapped underneath the graphene by leaving the devices at an angle during drying.

Considering the SEM images in Figure 8, it seems that more impurities were left on the substrate which was cleaned with boiling acetone. The presence of black dots – possibly dirt particles – on the acetone-cleaned device and the corresponding absence of such on the RCA-cleaned substrate could suggest that the latter is a more efficient substrate cleaning method.

Looking at the Raman spectra in Figure 9 it can be said that the graphene quality is high and consistently so along all the devices. The hydrophilic device was not the only one which shifted to slightly higher Raman shift values (2696 cm^{-1}) but also the RCA-cleaned hydrophobic device had near-hydrophilic 2D-peak (2694 cm^{-1}). The latter is still not too different from the Raman shift values of the other hydrophobic, acetone-cleaned, device (2688 cm^{-1}). It could be that the slight difference between the 2D-peak values of the RCA- and acetone-cleaned devices is present just due to the differences in substrate cleaning methods, but it is more likely that the area measured for the RCA-cleaned device had more bilayers present, which caused a shift to the higher Raman shift values.

3.3.2 Direct formation of graphene from amorphous carbon

Even prior to the experiment it was evident that without a carbon source below the nickel catalyst there would not be nearly enough carbon available in the environment of the device to be absorbed in the metal and initiate graphene formation upon annealing. This seemed to be quite likely when in Figure 10 the optical microscope images post-annealing showed the Si-SiO_2-Ni device to have no darker islands in comparison to the Si-SiO_2-aC-Ni device. This postulation was further confirmed in Raman spectroscopy by the lack of 2D and G bands characteristic to graphene. Seemingly little to no carbon had been absorbed into the nickel from the surroundings of the device, thus rendering it impossible for graphene to form.

On the other hand, the Si-SiO_2-aC-Ni device was promising. As seen in the Raman spectra in Figure 13, the presence of the characteristic graphene bands confirmed the islands that formed on top of the nickel post-annealing were graphene. Moreover, due to the high intensity of the G peak and comparatively low intensity of the wide 2D peak, as well as the difference in colour intensity of the islands, it could be concluded that the graphene was not a monolayer but rather multilayer. Since the Raman spectra proved the amorphous carbon device had graphene on the nickel, it was necessary to check if graphene had formed underneath as well, and whether plasma etching the graphene on the nickel made a difference.

After etching the nickel, some graphene was still present on the device without prior plasma etching, but in much lower quantities than before. The initial reasoning was that when graphene formed at the interface of nickel and SiO_2 it had mostly attached to nickel rather that SiO_2, thus only a small amount of graphene was left on the substrate while the rest dissolved with the nickel during the etching process (Vishwakarma *et al.*, 2017). But, as the Raman spectra of the plasma-etched device revealed the absence of graphene below nickel, this reasoning seemed unlikely. It was apparent that the low amount of graphene present below the nickel of the device where the overlying graphene was not etched had not been there initially and rather floated down from the top graphene layer during the etching process. Perhaps the "bottom graphene layer" would not have been there if the devices were etched in an upright position thus not allowing the overlying graphene to attach itself to the substrate.

In further testing with the aC-Ni-Ti devices, graphene did not form on the device annealed in high vacuum. It was concluded that by using pressure of 10^{-5} to 10^{-6} mbar for annealing, the Ni-Ti layers had peeled off the device before the amorphous carbon could form graphene by absorbing and desorbing to and from nickel - the experiment with this device had thus failed. On the other hand, the aC-Ni-Ti device annealed in low vacuum had formed graphene, although the graphene was grainy, non-uniform and had large 50~200 µm-sized holes. Possibly the holes in the graphene were areas where the graphene had formed onto the top Ni layer rather than the underlying SiO_2 layer (Vishwakarma *et al.*, 2017).

As for the aim of the Ti carbon diffusion barrier – this Ti layer had undoubtedly assisted the graphene formation below the Ni layer since the amount of graphene present after etching of aC-Ni-Ti had greatly increased compared to the previous devices without a top Ti layer.

Considering the results of this experiment, it could be concluded that with this method no functional large-scale graphene was able to form on the necessary substrate without major defects occurring. Although it should be noted, the author remains hopeful that such aC devices

could form higher quality graphene if further experiments, such as optimizing the conditions for the annealing or using some method to make the SiO_2 surface instead of nickel more favourable for graphene formation, were done. Perhaps further research could minimize the defects in the graphene formed from amorphous carbon.

3.3.3 Graphene in functional resistive switching devices

In the present study, SiO_2 could not be grown on graphene via ALD since ozone must be used together with $Si_2(NHC_2H_5)_6$ as the established and reliably working oxygen precursor. O_3 could not be used upon deposition of metal oxide films on graphene due to the destructive effect of O_3 on graphene. At the same time, $Si_2(NHC_2H_5)_6$ does not react effectively with H_2O, which is otherwise the most used oxygen precursor in ALD. Graphene was completely removed from the substrate surface when exposed to ozone flow at any temperatures exceeding room temperature. For this reason, HfO_2 was deposited on graphene, instead of SiO_2, after pre-treatment of graphene during few cycles of TEMAH and H_2O, followed by the earlier established plasma-assisted HfO_2 process.

The presence of an interfacial TiO_2 layer (Figure 22 (b)) for the further electrical RRAM means the formation of an additional reservoir of defects at the electrode/switching oxide junction, which may not necessarily mean deterioration of the switching performance but lowering of switching voltages, i.e. increasing switching feasibility and uniformity.

Prior to discussing the resistive switching capacity of the devices, it is worth mentioning the quality of the graphene seen in the Raman spectra. Before the deposition of another oxide layer onto the transferred graphene, the structural integrity of the graphene in the SEM images (Figure 19) looks to be intact both on the given 50 µm scale as well as on a smaller scale (not shown). Due to the nature of the substrate, its background noise makes it difficult to discern whether a D peak is present in the Raman spectra (Figure 20) and how intense it is. But, as the D peak cannot be seen without further manipulation of the spectra it could be said that the graphene was of a high quality and the underlying ALD-made SiO_2 did not cause issues with the transferred graphene.

The quality of graphene in the SiO_2-graphene-HfO_2 stacks after deposition of the HfO_2 film was worse than before, as seen by the substantial increase in D peak intensity in Figure 21. Seemingly, the graphene structure did not favour the deposition of HfO_2 on it. It is worth noting that the high intensity of the D-band in graphene was possibly caused by the graphene bonding changing from sp^2 to sp^3 upon chemical reaction with newly-deposited HfO_2, and consequently

causing reduced intensity of the 2D peak (Niyogi *et al.*, 2010). When comparing the Raman spectra of the stacks with ALD-made HfO_2 to the stacks with SiO_2 deposited via EBE, the latter has far less defects and its graphene looks much more promising for functional resistive switching devices. Also, upon deposition of HfO_2 onto the graphene, it seemed that the non-annealed base stack had a higher quality graphene as the 2D to G peak ratio was higher (I_{2D}:I_G = 2.0) compared to the device with the annealed base stack (I_{2D}:I_G = 0.7).

As seen in Figure 23, the oxide stacks without graphene did not switch resistively, probably due to their markedly high dielectric strength. In such highly insulating structures, the resistive switching effect could not be instigated. On the other hand, Si-TiN-SiO_2-graphene-HfO_2-Ti device performance was quite different compared to that of devices without graphene.

The device with graphene and non-annealed base stack showed bipolar switching behaviour. However, the switching SET and RESET events, as well as the LRS and HRS levels were rather irregular as seen in Figure 24, suffering from abrupt changes in the switching direction (i.e. clockwise vs. counter clockwise), although inducing implications of multilevel resistive switching performance. Such a butterfly-like appearance of the resistive switching behaviour is likely indicative of considerable structural and chemical inhomogeneities in the solid medium subjected to switching. Introduction of intermediate graphene layer may serve as source of defects and increased conduction, promoting switching, but the quality of neighbouring oxide layers may not yet suffice for the provision of uniform switching in terms of both voltages and resistivity state ratios.

The device with graphene and annealed base stack showed improved switching uniformity (Figure 25). On the other hand, the LRS:HRS ratios (I_{LRS}:I_{HRS}) did not exceed 3-4 unlike the non-annealed device. Then again, the repeatability of the switching cycles, expressed as the difference between low and high resistivity states recorded during consecutive cycles and termed as the device endurance, was appreciable, extending over 500 cycles.

Comparing the non-annealed (Figure 23) and annealed (Figure 27) devices without graphene shows a substantial difference in the resistive switching capability. Although the graphene-less device with the annealed base stack was capable of switching, the stability of the low to high resistivity ratios examined and recorded on different devices, i.e. the top electrodes in the whole matrix, was clearly worse compared to that obtained while measuring the devices with graphene. When comparing endurance measurements the device containing graphene (Figure 26) provided more reliable courses of endurance, whereas the graphene-less device (Figure 28)

clearly indicated the decrement in the LRS:HRS ratio (I_{LRS}:I_{HRS}) upon application of sequential switching voltage pulses within a rather low number of switching cycles.

Somewhat surprising switching behaviour was observed in Si-TiN-SiO_2-graphene-SiO_2-Ti devices, where the first SiO_2 was grown by ALD on TiN, and the second SiO_2 film was electron beam evaporated onto the graphene (Figure 6). In this sample, at first, remarkable light-sensitivity was detected, expressed by considerable increment in the conduction currents under exposure to the ordinary laboratory lights. In addition, upon sweeping the voltage pulse bias along the voltage axis, shift in the zero current value was recorded under illumination (not shown), being indicative of the charge generation at zero bias, and thus a possibility to consider the Si-TiN-SiO_2-graphene-SiO_2-Ti stack as an embryonic solar cell.

Graphene has been considered as a useful constituent material as a transparent electrode in silicon based solar cell structures (Vaianella *et al.*, 2015; Altuntepe *et al.*, 2020; Torres *et al.*, 2021). In regard with SiO_2-based solar cells, graphene has also been studied as a component material, although even more rarely (Islam *et al.*, 2016).

Based on the results, one can consider the possibility, that tailoring graphene and otherwise well-insulating laminates might serve as an approach allowing resistive switching in materials with high dielectric strength.

SUMMARY

Based on the discussion of the results of the three experiments within this thesis, the following conclusions can be made for each experiment.

In the first experiment, the quality of transferred graphene was assessed as well as the effect of substrates with altered wettability and different cleaning methods.

Overall, the quality of graphene transferred with the wet chemical transfer method was excellent and its structural integrity was not altered by this method. SEM images in Figure 8 showed that the graphene did not have any major large-scale defects, aside from some minor impurities. Raman spectra in Figure 9 showed an absence of a D-peak and thus confirmed that the presence of impurities was so minuscule that it did not affect the overall graphene quality. As for the effect of the substrate cleaning method, it was quite clear from the SEM images that the RCA cleaning method (Figure 8 left) was superior as it contained less impurities compared to the boiling acetone cleaning method (Figure 8 right) which not only had more impurities, but also had some chemical stains. Lastly, the altered wettability of the substrate seemed to have no major difference on the quality of the transferred graphene that could be seen in the Raman spectra and SEM images did not show that the graphene on the hydrophobic substrate was more wrinkled than on the hydrophilic one. Although, it must be mentioned that transferring graphene onto a hydrophilic substrate is easier due to the increased adhesive properties between the substrate and graphene.

In the second experiment, the quality of graphene directly formed from a carbon source with the aid of a carbon diffusion layer was assessed as well as the effect of a carbon diffusion barrier on the formation of graphene at the interface of the substrate and carbon diffusion layer.

As expected, upon annealing amorphous carbon the carbon particles had dissolved into the nickel catalyst and crystallised into graphene when cooled, but the graphene was not a homogeneous monolayer as clearly visible in the optical microscope image in Figure 13. The Raman spectra in the same figure showed the presence of a D peak and a wide and splitting 2D peak, meaning that the graphene had formed as multilayer islands with low coverage and/or holes. The plasma etching of the graphene on top of nickel revealed that graphene had formed in significant quantities only above and not below the nickel layer (Figure 16), thus no appreciable amount of graphene was found on the substrate itself. The graphene formed in the aC-Ni device with a Ti carbon diffusion barrier had shown that it is possible to induce formation of graphene at the substrate-nickel interface, but the quality of such grainy, non-uniform

graphene with varied thickness, as seen in the SEM image of Figure 18, leaves much to be desired. The low intensity of the 2D peak and high intensity of the D peak seen in the Raman spectrum of the same figure affirms the poor quality of such directly formed graphene.

In the third and last experiment, the structural integrity of graphene transferred onto SiO_2 films was assessed before and after the deposition of another dielectric layer onto the graphene. Additionally, the effect of using graphene in such dielectric stacks, as well as the effect of heat-treating the base stack prior to graphene transfer was assessed and the resistive switching capabilities of these devices compared to analogous ones without graphene.

The SEM images in Figure 19, as well as the Raman spectra in Figure 20 showed that upon transferring the graphene onto SiO_2 films made with ALD, the structural integrity of the graphene was intact. Prior to the deposition of another oxide layer onto the graphene, there was no major difference in the graphene quality caused by annealing of the base stack. The Raman spectra in Figure 21 A and B showed that post-deposition of HfO_2 on the graphene, the non-annealed base stack had a higher quality graphene as the I_{2D}:I_G ratio was comparatively higher to the device with the annealed base stack. It is clear that the deposition of top oxide layer in SiO_2-graphene-HfO_2 stacks caused the graphene to become highly defective either by introducing vacancies into the graphene or by changing the carbon bonds from sp^2 to sp^3 by reacting with the newly-deposited HfO_2, as suggested by Niyogi *et al.* (Niyogi *et al.*, 2010). Disregarding the latter speculation, the stack with SiO_2 deposited by EBE onto graphene was the most promising as it did not have a visible D peak in its spectra (Figure 21 C).

Considering the resistive switching capabilities of these dielectric stacks, the as-deposited SiO_2 stack without graphene showed no such ability (Figure 23), while its annealed equivalent could switch (Figure 27) it had a less stable LRS to HRS ratio when compared to devices where graphene was used. Despite the graphene quality being better in the non-annealed SiO_2-graphene-HfO_2 device, its bipolar switching was irregular (Figure 24), the SiO_2-graphene-HfO_2 device with the annealed base stack had a regular switching pattern (Figure 25). Overall, the author believes the SiO_2-graphene-SiO_2 device, where the bottom SiO_2 was deposited via ALD and the top was deposited via EBE, is the most promising. Despite the high switching voltages and the asymmetric current-voltage characteristics, noticeable in Figure 29, this device had the highest-quality graphene according to the Raman spectrum which would be beneficial if the switching ability could be improved.

Clearly, graphene had a positive effect on the switching capability of most of these functional resistive switching devices and thus should be further researched.

REFERENCES

Al Faruque, M.A. *et al.* (2021) 'A Review on the Production Methods and Applications of Graphene-Based Materials', *Nanomaterials*, 11(9), p. 2414. doi:10.3390/nano11092414.

Alazmi, A. *et al.* (2016) 'Comparative study of synthesis and reduction methods for graphene oxide', *Polyhedron*, 116, pp. 153–161. doi:10.1016/j.poly.2016.04.044.

Altuntepe, A., Seyhan, A. and Zan, R. (2020) 'Graphene for Si-based solar cells', *Journal of Molecular Structure*, 1200, p. 127055. doi:10.1016/j.molstruc.2019.127055.

Arroval, T. *et al.* (2016) 'Effect of substrate-enhanced and inhibited growth on atomic layer deposition and properties of aluminum–titanium oxide films', *Thin Solid Films*, 600, pp. 119–125. doi:10.1016/j.tsf.2016.01.024.

Banerjee, W., Liu, Q. and Hwang, H. (2020) 'Engineering of defects in resistive random access memory devices', *Journal of Applied Physics*, 127(5), p. 051101. doi:10.1063/1.5136264.

Celano, U. (2016) 'Filamentary-Based Resistive Switching', in Celano, U., *Metrology and Physical Mechanisms in New Generation Ionic Devices*. Cham: Springer International Publishing (Springer Theses), pp. 11–45. doi:10.1007/978-3-319-39531-9_2.

Di Bernardo, A. *et al.* (2017) 'p-wave triggered superconductivity in single-layer graphene on an electron-doped oxide superconductor', *Nature Communications*, 8(1), p. 14024. doi:10.1038/ncomms14024.

Ferrari, A.C. (2007) 'Raman spectroscopy of graphene and graphite: Disorder, electron–phonon coupling, doping and nonadiabatic effects', *Solid State Communications*, 143(1–2), pp. 47–57. doi:10.1016/j.ssc.2007.03.052.

Geim, A.K. and Novoselov, K.S. (2007) 'The rise of graphene', *Nature Materials*, 6(3), pp. 183–191. doi:10.1038/nmat1849.

Granneman, E. *et al.* (2007) 'Batch ALD: Characteristics, comparison with single wafer ALD, and examples', *Surface and Coatings Technology*, 201(22–23), pp. 8899–8907. doi:10.1016/j.surfcoat.2007.05.009.

Islam, M.J. *et al.* (2016) 'Modeling of graphene/SiO2/Si(n) based metal-insulator-semiconductor solar cells', in *2016 4th International Conference on the Development in the in*

Renewable Energy Technology (ICDRET). *2016 4th International Conference on the Development in the in Renewable Energy Technology (ICDRET)*, Dhaka, Bangladesh: IEEE, pp. 1–4. doi:10.1109/ICDRET.2016.7421491.

Kahro, T. *et al.* (2021) 'Hafnium Oxide/Graphene/Hafnium Oxide-Stacked Nanostructures as Resistive Switching Media', *ACS Applied Nano Materials*, 4(5), pp. 5152–5163. doi:10.1021/acsanm.1c00587.

Kalita, D. (2015). 'Graphene produced by chemical vapor deposition: From control and understanding of atomic scale defects to production of macroscale functional devices' 148. https://tel.archives-ouvertes.fr/tel-01689796.

Kern, W. (1990) 'The Evolution of Silicon Wafer Cleaning Technology', *Journal of The Electrochemical Society*, 137(6), pp. 1887–1892. doi:10.1149/1.2086825.

Kim, Keun Soo *et al.* (2009) 'Large-scale pattern growth of graphene films for stretchable transparent electrodes', *Nature*, 457(7230), pp. 706–710. doi:10.1038/nature07719.

Kim, K.-J. *et al.* (2018) 'Direct formation of graphene on dielectric substrate: Controlling the location of graphene formation adopting carbon diffusion barrier', *Journal of Vacuum Science & Technology B, Nanotechnology and Microelectronics: Materials, Processing, Measurement, and Phenomena*, 36(2), p. 021802. doi:10.1116/1.5016591.

Kukli, K. *et al.* (2020) 'Magnetic properties and resistive switching in mixture films and nanolaminates consisting of iron and silicon oxides grown by atomic layer deposition', *Journal of Vacuum Science & Technology A*, 38(4), p. 042405. doi:10.1116/6.0000212.

Kumar, R. *et al.* (2014) 'Graphene as a transparent conducting and surface field layer in planar Si solar cells', *Nanoscale Research Letters*, 9(1), p. 349. doi:10.1186/1556-276X-9-349.

Lee, J. *et al.* (2016) 'Tuning Ionic Transport in Memristive Devices by Graphene with Engineered Nanopores', *ACS Nano*, 10(3), pp. 3571–3579. doi:10.1021/acsnano.5b07943.

Li, X. *et al.* (2009) 'Large-Area Synthesis of High-Quality and Uniform Graphene Films on Copper Foils', *Science*, 324(5932), pp. 1312–1314. doi:10.1126/science.1171245.

Liu, Y. *et al.* (2017) 'Superconducting Continuous Graphene Fibers *via* Calcium Intercalation', *ACS Nano*, 11(4), pp. 4301–4306. doi:10.1021/acsnano.7b01491.

López, G.A. and Mittemeijer, E.J. (2004) 'The solubility of C in solid Cu', *Scripta Materialia*, 51(1), pp. 1–5. doi:10.1016/j.scriptamat.2004.03.028.

Lukose, R. *et al.* (2021) 'Influence of plasma treatment on SiO2/Si and Si3N4/Si substrates for large-scale transfer of graphene', *Scientific Reports*, 11(1), p. 13111. doi:10.1038/s41598-021-92432-4.

Mannequin, C. *et al.* (2016) 'Graphene-HfO_2-based resistive RAM memories', *Microelectronic Engineering*, 161, pp. 82–86. doi:10.1016/j.mee.2016.04.009.

Matero, R., Haukka, S. and Tuominen, M. (2008) 'High Growth Rate SiO2 by Atomic Layer Deposition', *ECS Transactions*, 13(1), pp. 453–457. doi:10.1149/1.2911529.

Miao, C. *et al.* (2011) 'Chemical Vapor Deposition of Graphene', in Mikhailov, S. (ed.) *Physics and Applications of Graphene - Experiments*. InTech. doi:10.5772/15543.

Natesan, K. and Kassner, T.F. (1973) 'Thermodynamics of carbon in nickel, iron-nickel and iron-chromium-nickel alloys', *Metallurgical Transactions*, 4(11), pp. 2557–2566. doi:10.1007/BF02644258.

Nguyen, V.T. *et al.* (2013) 'Synthesis of multi-layer graphene films on copper tape by atmospheric pressure chemical vapor deposition method', *Advances in Natural Sciences: Nanoscience and Nanotechnology*, 4(3), p. 035012. doi:10.1088/2043-6262/4/3/035012.

Niyogi, S. *et al.* (2010) 'Spectroscopy of Covalently Functionalized Graphene', *Nano Letters*, 10(10), pp. 4061–4066. doi:10.1021/nl1021128.

Novoselov, K.S. *et al.* (2004) 'Electric Field Effect in Atomically Thin Carbon Films', *Science*, 306(5696), pp. 666–669. doi:10.1126/science.1102896.

Pei, S. and Cheng, H.-M. (2012) 'The reduction of graphene oxide', *Carbon*, 50(9), pp. 3210–3228. doi:10.1016/j.carbon.2011.11.010.

Peng, Z. *et al.* (2011) 'Direct Growth of Bilayer Graphene on SiO_2 Substrates by Carbon Diffusion through Nickel', *ACS Nano*, 5(10), pp. 8241–8247. doi:10.1021/nn202923y.

Ren, S., Rong, P. and Yu, Q. (2018) 'Preparations, properties and applications of graphene in functional devices: A concise review', *Ceramics International*, 44(11), pp. 11940–11955. doi:10.1016/j.ceramint.2018.04.089.

Saeed, M. *et al.* (2020) ‘Chemical Vapour Deposition of Graphene—Synthesis, Characterisation, and Applications: A Review’, *Molecules*, 25(17), p. 3856. doi:10.3390/molecules25173856.

Slesazeck, S. and Mikolajick, T. (2019) ‘Nanoscale resistive switching memory devices: a review’, *Nanotechnology*, 30(35), p. 352003. doi:10.1088/1361-6528/ab2084.

Song, Y. *et al.* (2021) ‘Graphene Transfer: Paving the Road for Applications of Chemical Vapor Deposition Graphene’, *Small*, 17(48), p. 2007600. doi:10.1002/smll.202007600.

Sun, B. *et al.* (2021) ‘Multistate resistive switching behaviors for neuromorphic computing in memristor’, *Materials Today Advances*, 9, p. 100125. doi:10.1016/j.mtadv.2020.100125.

Torres, I. *et al.* (2021) ‘Graphene-Based Electrodes for Silicon Heterojunction Solar Cell Technology’, *Materials*, 14(17), p. 4833. doi:10.3390/ma14174833.

Tung, T.T. *et al.* (2016) ‘Graphene Oxide-Assisted Liquid Phase Exfoliation of Graphite into Graphene for Highly Conductive Film and Electromechanical Sensors’, *ACS Applied Materials & Interfaces*, 8(25), pp. 16521–16532. doi:10.1021/acsami.6b04872.

Vaianella, F., Rosolen, G. and Maes, B. (2015) ‘Graphene as a transparent electrode for amorphous silicon-based solar cells’, *Journal of Applied Physics*, 117(24), p. 243102. doi:10.1063/1.4923232.

Vishwakarma, R. *et al.* (2017) ‘Transfer free graphene growth on SiO_2 substrate at 250 °C’, *Scientific Reports*, 7(1), p. 43756. doi:10.1038/srep43756.

Warner, J.H. *et al.* (2013) ‘Characterisation Techniques’, in *Graphene*. Elsevier, pp. 229–332. doi:10.1016/B978-0-12-394593-8.00005-9.

Ye, C. *et al.* (2016) ‘Physical Mechanism and Performance Factors of Metal Oxide Based Resistive Switching Memory: A Review’, *Journal of Materials Science & Technology*, 32(1), pp. 1–11. doi:10.1016/j.jmst.2015.10.018.

Yi, M. and Shen, Z. (2015) ‘A review on mechanical exfoliation for the scalable production of graphene’, *Journal of Materials Chemistry A*, 3(22), pp. 11700–11715. doi:10.1039/C5TA00252D.

Zagwijn, P.M. *et al.* (2008) 'Novel Batch Titanium Nitride CVD Process for Advanced Metal Electrodes', *ECS Transactions*, 13(1), pp. 459–464. doi:10.1149/1.2911530.

Appendix

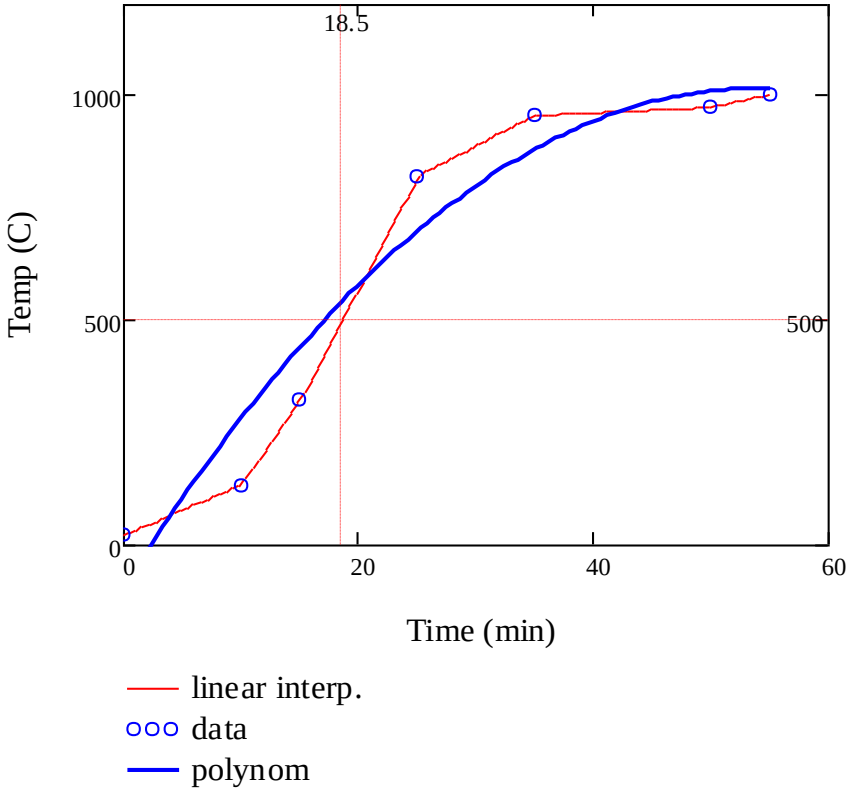

Figure I. Graph of the temperature-time dependence in a CVD reactor. Calculated heating rate from room temperature to 500 °C is 27 °C/min, from room temperature to 1000 °C is 17.8 °C/min, and from 500 °C to 1000 °C is 13.7 °C/min.

NON-EXCLUSIVE LICENCE TO REPRODUCE THESIS AND MAKE THESIS PUBLIC

I, Kristina Raudonen,

(*author's name*)

1. grant the University of Tartu a free permit (non-exclusive licence) to

reproduce, for the purpose of preservation, including for adding to the DSpace digital archives until the expiry of the term of copyright, my thesis

SYNTHESIS, ANALYSIS, AND APPLICATION OF GRAPHENE LAYERS FOR FUNCTIONAL DEVICES,

(*title of thesis*)

supervised by Dr. Kaupo Kukli and Mr. Tauno Kahro.

(*supervisors names*)

2. I grant the University of Tartu a permit to make the work specified in point 1 available to the public via the web environment of the University of Tartu, including via the DSpace digital archives, under the Creative Commons licence CC BY NC ND 4.0, which allows, by giving appropriate credit to the author, to reproduce, distribute the work and communicate it to the public, and prohibits the creation of derivative works and any commercial use of the work until the expiry of the term of copyright.

3. I am aware of the fact that the author retains the rights specified in points 1 and 2.

4. I confirm that granting the non-exclusive licence does not infringe other persons' intellectual property rights or rights arising from the personal data protection legislation.

Kristina Raudonen

27/05/2022